This is the peer reviewd version of the followng article:

Development of a RANS-Based Knock Model to Infer the Knock Probability in a Research Spark-Ignition Engine / D'Adamo, A., Breda, S., Iaccarino, S., Berni, F., Fontanesi, S., Zardin, B., Borghi, M., Irimescu, A., Merola, S.. - In: SAE INTERNATIONAL JOURNAL OF ENGINES. - ISSN 1946-3936. - 10:3(2017), pp. 1-18. [10.4271/2017-01-0551]

Terms of use:

The terms and conditions for the reuse of this version of the manuscript are specified in the publishing policy. For all terms of use and more information see the publisher's website.

16/11/2026 20:18

(Article begins on next page)

Development of a RANS-based Knock Model to Infer the Knock Probability in a Research Spark-Ignition Engine

Author, co-author (Do NOT enter this information. It will be pulled from participant tab in MyTechZone)

Affiliation (Do NOT enter this information. It will be pulled from participant tab in MyTechZone)

Abstract

Engine knock is one of the most limiting factors for modern Spark-Ignition (SI) engines to achieve high efficiency targets. The stochastic nature of knock in SI units hinders the predictive capability of RANS knock models, which are based on ensemble averaged quantities.

To this aim, a knock model grounded in statistics was recently developed in the RANS formalism. The model is able to infer a presumed log-normal distribution of knocking cycles from a single RANS simulation by means of transport equations for variances and turbulence-derived probability density functions (PDFs) for physical quantities. As a main advantage, the model is able to estimate the earliest knock severity experienced when moving the operating condition into the knocking regime.

In this paper, improvements are introduced in the model, which is then applied to simulate the knock signature of a single-cylinder 400cm^3 direct-injection SI unit with optical access; the engine is operated with two spark timings, under knock-safe and knocking conditions respectively. The statistical prediction of knock resulting from the presented knock model is compared to the experimental evidence for both investigated conditions.

The agreement between the predicted and the measured knock distributions validates the proposed knock model. Finally, limitations and some unprecedented possibilities given by the model are critically discussed, with particular emphasis on the meaning of RANS knock prediction.

Introduction

Engine knock is the object of a huge number of studies in the recent years, as it constitutes one of the main barriers limiting the increase of efficiency for modern SI units [1,2]. Knock is caused by the self-ignition of a portion of unburnt mixture before the main flame front initiated by the spark-plug regularly consumes it in deflagration mode. The sudden and simultaneous heat release of the remaining end-gas mixture may trigger a detonating pressure wave within the combustion chamber and severely damage engine components, thus preventing engine reliability. Knock-safe conditions are typically pursued through a combination of boosting limitation, charge enrichment and SA reduction. All these remedies relevantly affect engine-out performance and efficiency.

From a modelling standpoint, the stochastic nature of engine knock, related to combustion instability and cycle-to-cycle variability (CCV) of turbulent flows, would suggest Large-Eddy Simulation (LES) as the most appropriate approach for CFD simulations. Despite this is conceptually true and several publications show the applicability of LES to both research and production units [3-9], LES still remains a very demanding approach which can hardly be integrated in the industrial design process for the development of new SI units.

To limit computational costs and times, RANS models are usually chosen to represent the average engine behavior. Several successful knock models are available in literature to predict average knock onset in SI engines [10,11], though they all suffer from the intrinsic inability to account for far-from-average realizations. This limitation can be overcome by the use of variance equations for fundamental physical variables in RANS, such as in the models proposed by Linse et al. [12] and by the authors [13]. The information given by this kind of models is of statistical nature and it is grounded in turbulence-generated variance of physical fields, which in turn affects the end-gas reaction rate towards autoignition. Conversely from LES, these models naturally neglect a series of CCV-promoting factors, e.g. those pertaining to variability in spark-ignited flame kernel onset and turbulent flame propagation variability. However, such statistics-based RANS models are able to artificially reconstruct a presumed probability of knocking cycles, which can be a very useful indication to the engine designer. Finally, the presumed probability of knocking cycles deriving from this family of models can be correlated to the response of knock controllers, allowing a physically more robust knock analysis than that using consolidated models based on average quantities only.

In [13] the authors proposed an early version of such PDF-based knock model, considering the in-cell variation of temperature and mixture fraction. This was the basis for a Gaussian representation of knock onset probability, and ultimately for the reconstruction of a presumed fraction of knocking cycles. In the present paper, the PDF-knock model is further developed and several improvements are introduced. A first one involves the statistical link for the in-cell conditions between temperature and mixture quality variations: a dynamically calculated correlation coefficient between mean fields of mixture fraction and temperature is now introduced.

A second one is the function used for the knock probability reconstruction. In particular, log-normal distributions are adopted as the most representative univariate distribution function for knock onset. Similar distributions were used in several experimental studies

analyzing knock onset results, such as those by Peyton Jones and co-workers [14-19]. They demonstrated that for low-to-moderate knock intensities, engine knock is essentially a cyclically independent phenomenon and no cycle-to-cycle correlation is present for a wide variety of engine speeds and loads. Independently of the metrics used to identify knock intensity, log-normal distribution is found to be a good candidate to represent the rate of probability of knocking events of a given severity. In fact, a vast majority of the population of cycles usually lies in a restricted region around the mean knock intensities, though a "longer tail" of sporadic but damaging knocking individuals is observed. This becomes more and more relevant as the engine operating condition is moved towards knock-affected conditions and the distribution of knock intensities becomes more and more spread. The fraction of knocking cycles is found to increase rapidly with SA increase, thus preventing the engine operation at edge-of-knock conditions. Such behavior was observed for several engine conditions, either knock-safe and knocking ones; in order to describe this evidence some kind of non-symmetrical distribution function is needed. In this framework, log-normal functions were found to be a useful tool. Finally, the related Cumulative Density Function (CDF) is used to describe the overall probability to exceed a predefined knocking threshold, which can be easily related to the fraction of knocking cycles.

In the next Section, the PDF-Knock model details are reported, with particular care to the modelling improvements introduced from the model in [13]. Then the model will be applied at first to a simple test case, to highlight all the main parameters behavior, and then to a research engine tested at different SA. Finally, considerations on the knock probability presumed distribution indicated by the PDF-Knock model will be critically discussed.

PDF-Knock Model

The presented PDF-Knock model is a development of the approach proposed originally in [13]. It is recalled here in its fundamentals, together with the description of the model improvements.

Motivations for the PDF-Knock Model

The standard approach to knock modelling considers the Livengood-Wu knock precursor I [20] to track the progress towards autoignition (Eq. 1); such approach is based on a unique cell-averaged ignition delay time $\tilde{\tau}$ and its inverse (i.e. the cell-averaged reaction rate $\widetilde{\omega}$). The AI delay time is calculated using the look-up table approach proposed by the authors [10] which considers $\tilde{\tau}$ as a function of mean cell quantities, i.e. $\tilde{\tau} = \tilde{\tau}\left(\tilde{p}, \tilde{T}_u, \widetilde{\Phi}, \tilde{Y}_{EGR}\right)$. To this aim, an indexed look-up table containing chemistry calculated ignition delay times from a detailed chemical mechanism is generated off-line and it is recalled during the CFD run.

$$I = \int_{t_0}^{t} \widetilde{\omega}\, dt = \int_{t_0}^{t} \frac{1}{\tilde{\tau}} dt \qquad (1)$$

However, this framework fails if in-cell variability of physical states is considered, since a global cell-averaged reaction rate $\widetilde{\omega}$ is not uniquely defined. To overcome this limitation, the use of multiple knock precursors will be advocated.

PDF-Knock Model Equations

As stated before, the model is based on two additional transport equations for the variance of both mixture fraction Z and temperature T. Since both quantities affect the local AI delay time, it is inferred that their statistical variance (if present) should have an impact also on the in-cell description of the AI reaction rate.

The two additional transport equations for the variance of Z and T, Z' and T_u' respectively, are reported below (Eq. 2 and 3).

$$\frac{\partial \rho Z'}{\partial t} + \frac{\partial}{\partial x_j}\left[\rho v_j Z' - \left(\rho D_{Z'} + \frac{\mu_t}{\sigma_t}\right)\frac{\partial Z'}{\partial x_j}\right] = 2\frac{\mu_t}{\sigma_t}\left(\frac{\partial Z}{\partial x_j}\right)^2 - c_t \rho \frac{\varepsilon}{k} Z' \qquad (2)$$

$$\frac{\partial \rho T_u'}{\partial t} + \frac{\partial}{\partial x_j}\left[\rho v_j T_u' - \left(\rho D_{T_u'} + \frac{\mu_t}{\sigma_t}\right)\frac{\partial T_u'}{\partial x_j}\right] = 2\frac{\mu_t}{\sigma_t}\left(\frac{\partial T_u}{\partial x_j}\right)^2 - c_t \rho \frac{\varepsilon}{k} T_u' \qquad (3)$$

It is to be noted that the Favre-averaged energy equation solved by the CFD code is in the form of sensible enthalpy, from which the conversion to temperature is possible thanks to the local mixture specific heat. This is calculated based on local species composition. As for energy variance, the temperature formulation (Eq. 3) is adopted. In Eq. 2 and 3 a fixed turbulent Schmidt number σ_t equal to 0.9 is used. These equations differ from their counterparts for the mean quantities $\tilde{Z}$ and $\widetilde{T_u}$ in the right-hand side (RHS) terms, formally source terms for the variance equations.

The first RHS contribution is a positive source (i.e. variance generation) and it accounts for variance produced by the spatial gradient of the variable. The second RHS term describes variance dissipation, which is a function of a turbulent relaxation time-scale time scale τ_t, reported in Eq. 4:

$$\tau_t = \frac{1}{c_t(Re_t)} \cdot \frac{k}{\varepsilon} \qquad (4)$$

The characteristic turbulent time-scale of the $k-\varepsilon$ turbulence model (i.e. k/ε) is multiplied by a model constant $c_t(Re_t)^{-1}$. This is calculated as a monotonic increasing function of the local turbulent Reynolds number Re_t, as suggested by Fox [21] and by Subramanian et al. [22]. The $c_t(Re_t)$ value is cell-wise calculated from the curve reported in Figure 1.

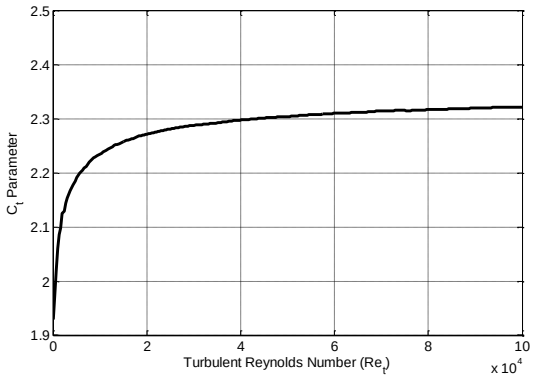


Figure 1. Variance dissipation parameter $c_t(Re_t)$.

Low turbulent level (i.e. low Re_t) implies a small value of $c_t(Re_t)$, this in turn resulting in a long turbulent relaxation time-scale τ_t from Eq. 4. As a consequence, the variance destruction operated by turbulent mixing in Eq. 2 and 3 is slow and the probability to find far

from average in-cell states is high. The opposite situation characterizes highly turbulent conditions, where intense thermo-mechanical turbulent mixing leads to high $c_t(Re_t)$ values, low relaxation time-scale τ_t and a rapid and effective variance destruction; the system moves therefore towards a perfectly stirred status. Finally, the variance dissipation source term is proportional to the variance intensity itself.

Statistical Model for the In-Cell Conditions

In a perfectly homogeneous field, the first RHS term would be null, since no variable gradients are present and variance could not be generated. In the same situation, there would be no possible variance dissipation as well, since this would be proportional to the variance itself. To satisfy both conditions, variance must be identically null in every point. This describes the variance equations behavior for a singular case such as a perfectly homogeneous field. For inhomogeneous fields, both the first and the second moments (i.e. the mean and the variance) for mixture fraction Z and unburnt temperature T_u are generally not null. As presented in [13], the joint variation of both variables may be represented as a simplified Gaussian bi-variate distribution model, expressed by Eq. 5:

$$P(Z,T) = \frac{1}{2\pi\cdot\sigma_Z\sigma_{T_u}}\cdot exp\left\{-\frac{1}{2}\cdot\left[\frac{(Z-\bar{Z})^2}{{\sigma_Z}^2}+\frac{(T_u-\bar{T}_u)^2}{{\sigma_{T_u}}^2}\right]\right\} \quad (5)$$

However, Eq. 4 is valid under the assumption of uncorrelated Z and T_u variables, which is an unlikely scenario for modern GDI units, where intense fuel stratification is observed. Charge stratification usually persists until the end of the compression stroke, and it causes temperature inhomogeneity due to the dependency of the specific heat on mixture quality.

In the present paper the model is improved by considering a more refined scenario where this correlation exists and influences the shape of the bi-variate statistical model for the in-cell physical states.

To this aim, the model is evolved by considering the general formulation for bi-variate Gaussian distribution, reported in Eq. 6 and by introducing a correlation coefficient ρ_{ZT}:

$$P(Z,T) = \frac{1}{2\pi\cdot\sigma_Z\sigma_{T_u}\cdot\sqrt{1-{\rho_{ZT}}^2}}\cdot exp\left\{-\frac{1}{2(1-{\rho_{ZT}}^2)}\cdot\left[\frac{(Z-\bar{Z})^2}{{\sigma_Z}^2}+\frac{(T_u-\bar{T}_u)^2}{{\sigma_{T_u}}^2}-\frac{2\rho_{ZT}(Z-\bar{Z})(T_u-\bar{T}_u)}{\sigma_Z\sigma_{T_u}}\right]\right\} \quad (6)$$

This formulation accounts for correlated Z and T_u variables. The correlation coefficient ρ_{ZT} is calculated in the model at each iteration through the analysis of the in-cylinder instantaneous $\tilde{Z}$ and $\widetilde{T_u}$ fields and it is modelled using a Pearson-like formulation as in Eq. 7:

$$\rho_{ZT} = \frac{\sigma_{ZT}}{\sigma_{\tilde{Z}}\cdot\sigma_{\widetilde{T_u}}} = \frac{\sum_i\left[(Z_i-\langle Z\rangle)\cdot(T_{u,i}-\langle T_u\rangle)\right]}{\sqrt{\sum_i(Z_i-\langle Z\rangle)^2}\cdot\sqrt{\sum_i\left(T_{u,i}-\langle T_u\rangle\right)^2}} \quad (7)$$

In Eq. 7, the $\sigma_{\tilde{Z}}$ and $\sigma_{\widetilde{T}}$ terms are the standard deviation of the mean in-cylinder $\tilde{Z}$ and $\widetilde{T_u}$ fields. Therefore, the ρ_{ZT} coefficient is dynamically calculated at each iteration based on the instantaneous modeled mean $\tilde{Z}$ and $\widetilde{T_u}$ fields and it is found to be always negative: high $\tilde{Z}$ cell-values (i.e. rich-in-fuel regions) are more likely associated to low $\widetilde{T_u}$. This is an expected consequence of the relationship between $\tilde{Z}$ and $\widetilde{T_u}$ deriving from the mixture isobaric specific heat. The instantaneous local ρ_{ZT} correlation coefficient modifies the bi-variate Gaussian model for the in-cell conditions as illustrated in Figure 2 for several ρ_{ZT} parameter values. In Figure 2 the equivalence ratio is used instead of $\tilde{Z}$ to represent fuel concentration. Hotter states are associated with leaner mixtures (bottom-right side in Figure 2) and the same is for cooler and richer conditions (upper-left side in Figure 2), while hot and rich (upper-right) or cool and lean (lower-left) combinations are less probable.

Finally, it is noted that bi-variate Gaussian distribution is one of the possible models for the cell reactor model and it could be substituted by bi-variate beta-distribution. The authors choice of bi-variate Gaussian distribution is motivated by its relative simplicity and its robust representation of in-cell distribution of states.

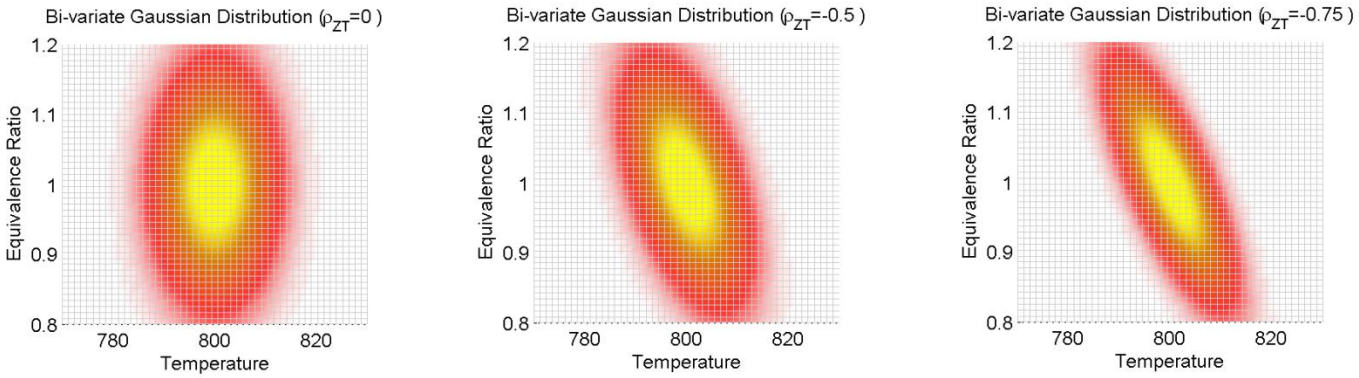


Figure 2. Bi-variate Gaussian distribution for the in-cell statistical states as a function of the ρ_{ZT} correlation coefficient: $\rho_{ZT} = 0$ (left, uncorrelated equivalence ratio and T_u), $\rho_{ZT} = -0.5$ and $\rho_{ZT} = -0.75$ (middle and right, negatively correlated equivalence ratio and T_u).

Statistical Model for the In-Cell Reaction Rate

Given the outlined model to represent the statistical distribution of in-cell conditions, a similar treatment based on first and second moments is pursued for the description of the reaction rate distribution.

In fact, once in-cell variability of physical states is introduced, a unique cell-averaged ignition delay time $\tilde{\tau}$ (or the cell-averaged reaction rate $\widetilde{\omega}$) is not sufficiently representative of the cell reactivity states. To overcome this limitation, multiple knock precursors are adopted.

The mean ignition delay $\tau_{PDF-aver}$ is calculated as the PDF-weighted average of the ignition delay times of all the in-cell represented conditions (Eq. 8), from which a cell-average reaction rate $\omega_{PDF-aver}$ is derived (Eq. 9).

$$\tau_{PDF-aver} = \sum_{i=1}^{Z_{tot}} \sum_{j=1}^{T_{u,tot}} P(Z_i, T_{u,j}) \cdot \tau(Z_i, T_{u,j})\, dZ dT_u \tag{8}$$

$$\omega_{PDF-aver} = {\tau_{PDF-aver}}^{-1} \tag{9}$$

The weighting operator is the bi-variate Gaussian model reported in Eq. 6, accounting for $\widetilde{Z}$ and $\widetilde{T_u}$ mutual correlation through ρ_{ZT} (Eq. 7). The role of the $\omega_{PDF-aver}$ term is similar to the standard reaction rate for the knock precursor in RANS knock models, i.e. conceptually accounting for the mean precursor growth towards knock as if the entire cell was at its Favre-average status. It is however to be noted that even if $\omega_{PDF-aver}$ is a mean term, it is calculated by weighting on all the represented states in the cell, hence non-linear τ variation are considered.

As a second step, a variance-like variable must be introduced to represent the reaction rate distribution around the PDF-weighted average value. However, differently from the previous model implementation in [13], attention is paid to the reaction rate distribution emerging from this treatment. In fact, different variance amplitudes are encountered if distribution spread is calculated on the faster or slower-than-average states: in other words, the in-cell distribution of reaction rates does not rigorously follow a normal distribution. This is due to the rapid AI delay decrease when entering in the medium-to-high temperature chemistry, while much slower reacting states are still present for slightly lower T_u. As a model improvement, this behavior is accounted for by two conditioned variances calculated for each cell: one for the faster-than-average states and one for the slower-than-average, $\sigma_{\tau,-\sigma}$ and $\sigma_{\tau,+\sigma}$ respectively (Eq. 10 and 11).

$$\sigma_{\tau,-\sigma} = \sqrt{\frac{1}{N}(\tau_i - \tau_{PDF-aver})^2}\Big|_{\tau_i<\tau_{PDF-aver}} \tag{10}$$

$$\sigma_{\tau,+\sigma} = \sqrt{\frac{1}{N}(\tau_i - \tau_{PDF-aver})^2}\Big|_{\tau_i>\tau_{PDF-aver}} \tag{11}$$

Based on these quantities, it is possible to calculate the net difference in reaction rate from the mean value $\omega_{PDF-aver}$. Two variables are used for this, $\tau_{-\sigma}$ and $\tau_{+\sigma}$ respectively, representing the ignition delay difference from the mean value $\tau_{PDF-aver}$ and calculated as in Eq. 12 and 13.

$$\tau_{-\sigma} = \tau_{PDF-aver} - \sigma_{\tau,-\sigma} \tag{12}$$

$$\tau_{+\sigma} = \tau_{PDF-aver} + \sigma_{\tau,+\sigma} \tag{13}$$

Finally, two reactions rates are calculated, $\omega_{-\sigma}$ and $\omega_{+\sigma}$, representing the reaction rate acceleration and slow-down with respect to the mean $\omega_{PDF-aver}$ (Eq. 14 and 15).

$$\omega_{-\sigma} = \frac{1}{\tau_{-\sigma}} - \frac{1}{\tau_{PDF-aver}} = \frac{\tau_{PDF-aver} - \tau_{-\sigma}}{\tau_{PDF-aver} \cdot \tau_{-\sigma}} \tag{14}$$

$$\omega_{+\sigma} = \frac{1}{\tau_{+\sigma}} - \frac{1}{\tau_{PDF-aver}} = \frac{\tau_{PDF-aver} - \tau_{+\sigma}}{\tau_{PDF-aver} \cdot \tau_{+\sigma}} \tag{15}$$

Since $\omega_{-\sigma}$ is a positive contribution, being $\tau_{PDF-aver} > \tau_{-\sigma}$, it represents a reaction rate deviation towards an earlier autoignition event. By the same rationale, $\omega_{+\sigma}$ is a negative contribution, since $\tau_{PDF-aver} < \tau_{+\sigma}$, and it accounts for a statistically existing reduced reaction rate.

As last step, three independent knock precursors are transported, all based on a Livengood-Wu model. The first knock precursor $I_{PDF-aver}$ represents a Livengood-Wu model for the cell-average reaction rate, whose transport equation is Eq. 16:

$$\frac{\partial \bar{\rho} I_{PDF-aver}}{\partial t} + \nabla \cdot (\bar{\rho}\tilde{v} I_{PDF-aver}) = \nabla \cdot (\bar{\rho}(D + D_T)\nabla I_{PDF-aver}) + \\ + \bar{\rho}\omega_{PDF-aver} \tag{16}$$

The other two reaction rates, $I_{-\sigma}$ and $I_{+\sigma}$, follow a similar modeling approach, the only conceptual difference with $I_{PDF-aver}$ being their meaning: they represent the net difference of the knock precursor from the average one. Their transport equations are Eq. 17 and 18, and their source terms are $\omega_{-\sigma}$ and $\omega_{+\sigma}$ (Eq. 14 and 15) respectively. These are calculated based on turbulence-generated deviation of physical states (and consequently of AI delay times), hence they are dependent upon flow features only and not derived by user-imposed alteration of fields.

$$\frac{\partial \bar{\rho} I_{-\sigma}}{\partial t} + \nabla \cdot (\bar{\rho}\tilde{v} I_{-\sigma}) = \nabla \cdot (\bar{\rho}(D + D_T)\nabla I_{-\sigma}) + + \bar{\rho}\omega_{-\sigma} \tag{17}$$

$$\frac{\partial \bar{\rho} I_{+\sigma}}{\partial t} + \nabla \cdot (\bar{\rho}\tilde{v} I_{+\sigma}) = \nabla \cdot (\bar{\rho}(D + D_T)\nabla I_{+\sigma}) + + \bar{\rho}\omega_{+\sigma} \tag{18}$$

In the next Section it will be shown how the introduced knock precursors are used to reconstruct a presumed probability of knocking cycles.

Probability of Knocking Cycles

As stated in the Introduction, the analysis of knocking conditions is severely limited by the underlying assumptions of the RANS formalism, namely the phase-averaging of Navier-Stokes equations preventing a detailed simulation of stochastic events which can only be accounted for by statistical models.

In [13] the authors used the mean knock precursor and its variance to define a PDF distribution of knocking cycles. From this, a CDF was calculated to presume a probability of knocking cycles.

In this study the PDF-Knock model is evolved from [13] by considering log-normal distribution as a more consistent representation than normal Gaussian shape, as outlined in the

Introduction section [14,15]. Log-normal distribution of probability $P(x)$ of a strictly positive x variable is defined as in Eq. 19:

$$P(x) = \frac{1}{x \cdot \sigma\sqrt{2\pi}} \cdot e^{-\frac{(\ln x - \mu)^2}{2\sigma^2}} \quad (19)$$

In Eq. 19 μ and σ are the mean and standard deviation of the $\ln(x)$ distribution, and they represent a location and a scale parameter. The mean value and the standard deviation of x, M and ν respectively, are defined as Eq. 20 and 21.

$$M = e^{\mu + \frac{\sigma^2}{2}} \quad (20)$$

$$\nu = \left(e^{\sigma^2} - 1\right) \cdot e^{2\mu + \sigma^2} \quad (21)$$

Therefore, a method is proposed to correlate CFD results to distribution parameters. This is based on two knock phasing indicators, $MFU_{\overline{KO}}$ and $MFU_{KO'}$: they both express the residual unburnt fuel fraction at knock onset. As for $MFU_{\overline{KO}}$, it is related to the average knock phasing: it represents the unburnt fraction at mean knock onset as indicated by the $I_{PDF-aver}$ precursor reaching unity value. Similarly, $MFU_{KO'}$ regards the same quantity at knock onset as indicated by the $I_{-\sigma}$ precursor. Given the three-dimensional nature of the $I_{PDF-aver}$ and $I_{-\sigma}$ fields, knock onset is considered as the instant at which $I_{PDF-aver}$ or $I_{-\sigma}$ exceed 1 mm^3 of volume with value higher than unity.

Coherently with the RANS meaning for mean and variance, the mean value M is taken as the residual burnt fraction at knock onset, i.e. $MFU_{\overline{KO}} = 1 - MFB_{\overline{KO}}$, while the standard deviation ν is given by the difference in burnt fraction between the earliest knock onset KO' and the mean one $\overline{KO}$. Therefore the linear system (Eq. 22 and 23) is defined as:

$$M = MFU_{\overline{KO}} = e^{\mu + \frac{\sigma^2}{2}} \quad (22)$$

$$\nu = MFU_{KO'} - MFU_{\overline{KO}} = \left(e^{\sigma^2} - 1\right) \cdot e^{2\mu + \sigma^2} \quad (23)$$

The two equation system in two unknowns (μ and σ) is solved and expressions for the log-normal parameters are obtained as Eq. 24 and 25, describing a presumed log-normal distribution of knocking events based on the PDF-Knock model outcomes $MFU_{KO'}$ and $MFU_{\overline{KO}}$.

$$\sigma = \sqrt{ln\left[1 + MFU_{KO'} \cdot e^{-2 \cdot ln\left(MFU_{\overline{KO}}\right)}\right]} \quad (24)$$

$$\mu = ln(MFU_{\overline{KO}}) - \frac{\sigma^2}{2} \quad (25)$$

Finally, the fraction of knocking cycles is calculated as the Cumulative Density Function (CDF) of Eq. 19, expressed by Eq. 26:

$$CDF(x) = \frac{1}{2} \cdot \left[1 + erf\left(\frac{\ln x - \mu}{\sigma \cdot \sqrt{2}}\right)\right] \quad (26)$$

This represents the cumulative probability to have knocking events for a given MFU_{KO}. Since many knock intensity indicators are used and their specific threshold are based on manufacturers' experience, a more general knock severity indicator is assumed here as the MFU_{KO}. Knock intensity is commonly related to the residual burnt fraction at knock [23], and a distribution of this last can be used to infer an overall probability to record knocking events up to a given threshold. Finally, the complement to one is the cumulative probability to exceed such value, i.e. the statistical fraction of knocking cycles.

Given the model aim to comprehensively predict a presumed probability of knocking events, heat released by autoignition is numerically de-activated: it would be conceptually wrong to generate heat by one singular event (e.g. the earliest knock probability), thus altering the remaining realizations (e.g. the average knock onset) by thermodynamic effects.

PDF-Knock Model Test Case

A simple test case is illustrated in order to highlight the PDF-Knock model behavior for engine-typical conditions. A finite size rectangular plane is initialized with constant absolute pressure and temperature, 70 bar and 900 K respectively. As for species concentrations, a stoichiometric Gasoline field is imposed with no EGR presence.

The plane is initialized with increasing temperature variance T_u' on the x-direction, while increasing Z' is imposed on the y-direction. This variance initialization serves as a substitute of the transport equations for variances (Eq. 2 and 3 for T_u' and Z') and it is here adopted for test purposes only. The variance initial fields are illustrated in Figure 3.

As a result, the lower-left corner corresponds to a perfect-stirred reactor (PSR) condition (Point A) with no in-cell variance, while the upper-right corner to a highly variant condition (Point B). These are typical situations for high-turbulent (Point A) and low-turbulent states (Point B). The bi-variate PDF representing Point A and B states are represented in Figure 4. Given the identical mean Z and T_u fields used for this test case, the ρ_{ZT} correlation coefficient is not defined and the bi-variate model is built considering the simplified formulation for $\rho_{ZT} = 0$ (Eq. 5).

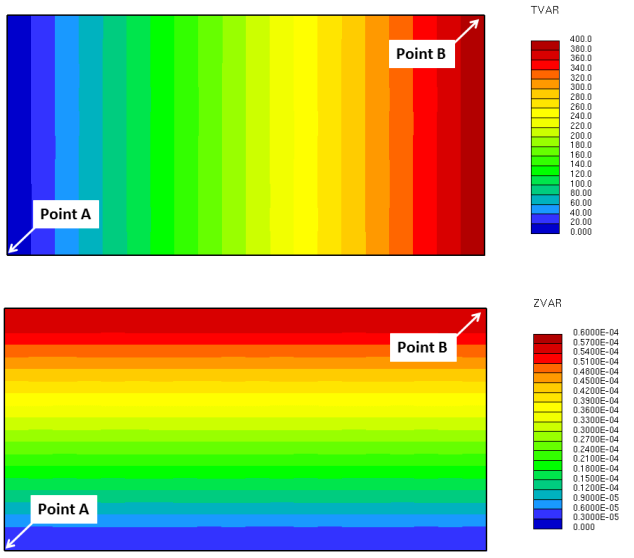


Figure 3. Variance initial fields for the test case: unburnt temperature variance T_u' (top) and mixture fraction Z' variance (bottom).

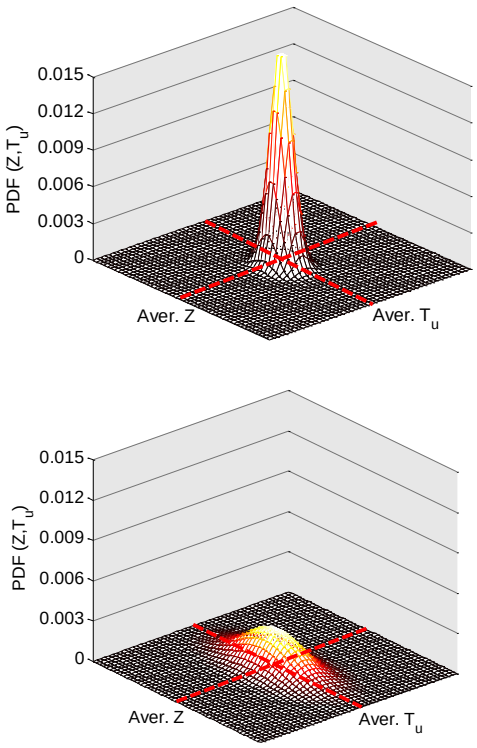


Figure 4. Probability Density Function of mixture fraction and unburnt temperature for Point A (Perfectly Stirred Reactor, top) and Point B (highly variant status, bottom).

Given the identical average pressure, temperature and mean mixture quality, the mean reaction rate for the analysed conditions would indicate a time to autoignition equal to 0.86 ms for a RON95 gasoline. However, the PDF treatment on temperature and mixture fraction considers the statistical deviation of such physical conditions from the mean values, hence a reaction rate distribution arises moving from Point A (equal reaction rate over the entire cell volume) to Point B.

In Figure 5 the PDF-weighted average delay time $\tau_{PDF-aver}$ and the separate standard deviations $\sigma_{\tau,-\sigma}$ and $\sigma_{\tau,+\sigma}$ are reported at 0.86 ms. It is visible that while $\tau_{PDF-aver}$ is roughly uniform, due to the identical mean conditions, AI delay variability is null at Point A and maximum at Point B.

The mean source term $\omega_{PDF-aver}$ field (Eq. 9) is represented in Figure 6 (left) and it is little affected by the increasing field variance moving from the lower-left to the upper-right corner. However, the in-cell presence of far-from-average states induces a reaction rate variance, represented in Figure 6 in terms of $\omega_{-\sigma}$ and $\omega_{+\sigma}$ respectively; both fields show null values at Point A (homogeneous PSR condition) and peak values at Point B (highly variant state). As previously underlined, $\omega_{-\sigma}$ has a positive sign while $\omega_{+\sigma}$ is negative.

The final result of the PDF treatment is that a statistically earlier knock onset is introduced together with the average knock prediction, and this depends on the variance amplitude. The knock precursor fields for the average knock precursor $I_{PDF-aver}$ is reported in Figure 7 at 0.9 ms, as well as its higher and lower values given by the $I_{-\sigma}$ and $I_{+\sigma}$ effect. As visible, the maximum deviation from the average knock prediction is experienced for highly variant states (Point B), while PSR-like conditions (Point A) are marginally affected by the PDF-treatment.

This simple test case shows the application of the PDF-knock model to typical unburnt mixture conditions, for increasing variance degrees. It demonstrates how the model is able to account for turbulence-generated variance of physical variables and how these may deviate knock onset from average knock prediction. Given the variability of local conditions in an engine and the degree of turbulence driving variance production and dissipation, a PDF-based approach appears as a more universal framework to account for possible far-from-average situations. The full PDF-Knock model application to a complete engine simulation is outlined in detail in the next Section.

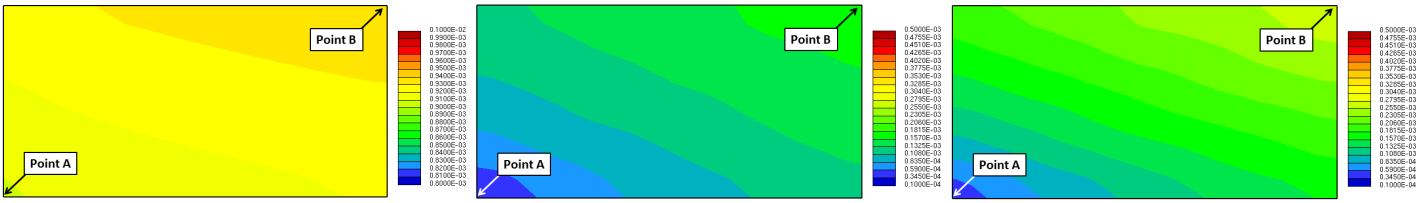


Figure 5. PDF-weighted average AI delay $\tau_{PDF-aver}$ field (left), standard deviation field for faster-than-average AI delay $\sigma_{\tau,-\sigma}$ (middle) and standard deviation field for slower-than-average AI delay $\sigma_{\tau,+\sigma}$ (right) at 0.9 ms.

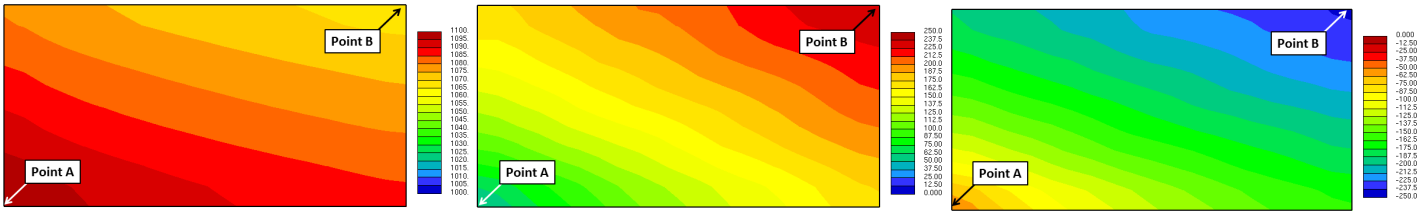


Figure 6. Field of average reaction rate $\omega_{PDF-aver}$ (left), field of faster-than-average reaction rate deviation $\omega_{-\sigma}$ (middle) and field of slower-than-average reaction rate deviation $\omega_{+\sigma}$ (right) at 0.9 ms.



Figure 7. Field of average knock precursor $I_{PDF-aver}$ (left), field of cumulative faster-than-average reaction rate ($I_{PDF-aver} + I_{-\sigma}$)(middle) and field of cumulative slower-than-average reaction rate ($I_{PDF-aver} + I_{+\sigma}$) (right) at 0.9 ms.

Experimental Apparatus

Measurements were performed on a single-cylinder optically accessible DISI engine, equipped with the cylinder head of a 1.4 litre currently produced SI turbocharged engine. Engine specifications are reported in [24,25] and only the main parameters (Table 1) are briefly resumed for the sake of completeness, along with the operating conditions. It should be noted that crank angle reference is made to the TDC at the end of compression. Fuel injection is operated by a wall-guided architecture featuring a side-mounted injector located in-between the intake valves. The fuel injector is a six-hole unit. The spark plug is centrally located. Optical access is obtained through an 18 mm-thick fused silica window fixed on the piston crown featuring a Bowditch design [26] with a 45 degree UV-enhanced mirror. The sequences of images were recorded using a CMOS camera at 5000 frames per second and 200 μs exposure time; the frame rate is equivalent to a resolution of 2.4 CAD at the chosen rotational speed of 2000 rev/min. Self-lubricating piston rings ensured oil-free operation in the optically accessible part, thus avoiding contamination of the visible field of view. Coolant and lubricant temperature were monitored and maintained at 330 K using a thermal conditioning unit.

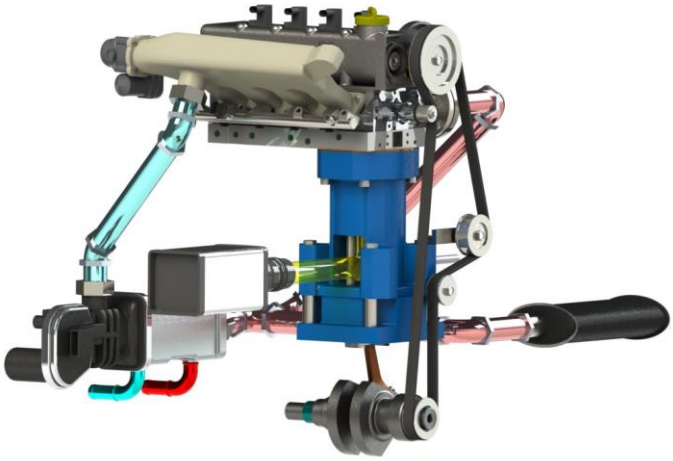


Figure 8. Sketch of the single-cylinder research engine with flat-piston optical access.

Table 1. Single cylinder SI engine characteristics.

Displacement	≈ 399 cm^3
Bore	79 mm
Stroke	81.3 mm
Connecting Rod Length	143 mm
Compression Ratio	10:1

Engine speed was set at 2000 rev/min, while start of injection was triggered at 300 CA bTDC with a single-pulse strategy at a pressure equal to 100 bar. The overall air-to-fuel ratio was set close to stoichiometry (λ≈1.05) and monitored using an oxygen sensor on the exhaust line, with an accuracy of ±1%. The experiments were carried out using a commercial RON95 gasoline for all the analyzed conditions.

Among the many available, two turbocharged operating conditions (OPs) are examined in this study, all with 0.5 bar boost pressure and intake manifold temperature around 315 K. The difference between them is the spark timing, which is varied from a knock-safe condition (SA=12 CA bTDC), to a knocking one (SA=15 CA bTDC). These will be hereafter named SA12 and SA15, respectively.

A sequence of 200 consecutive firing cycles was recorded for each OP and in-cylinder pressure traces are acquired by a flush-mounted fast-response pressure transducer with a 0.2 CA resolution, which is side-mounted between an intake and an exhaust valve. The cycle-resolved peak pressure values measured for each OP are reported in Figure 9.

The combustion variability for the two datasets is reported in Table 2, in terms of mean value, RMS and their ratio, expressed by the Coefficient of Variation (CoV).

Table 2. Variability of combustion indicators for the SA12 and SA15 OPs.

	SA12	SA15
MFB10	Mean=15.6 CA aSOC RMS=1.9 CA CoV=11.9%	Mean=14.8 CA aSOC RMS=1.4 CA CoV=9.5%
MFB50	Mean=23.6 CA aSOC RMS=2.31 CA CoV=9.8%	Mean=21.9 CA aSOC RMS=1.9 CA CoV=8.7%

The cycle-resolved Maximum Amplitude of Pressure Oscillation (MAPO) distributions acquired for the SA12 and SA15 OPs are reported in Figure 10, together with the MFB50 phasing indicators. Log-normal fits for both distributions are superimposed. It is clearly visible that for the lower SA condition (SA12) most of the cycles show MAPO values below 1 bar, and a relatively narrow and centered distribution is sufficient to reconstruct the MAPO distribution. For increased SA (SA15), several cycles exhibit MAPO values from 1 to 3 bar, and sporadic outlier cycles above 3 bar are present as well.

A threshold equal to 2 bar is chosen to discern between regular combustion noise and knock: the SA12 condition is knock-safe and is

labelled as the Knock-Limit Spark Advance (KLSA) one, while the SA15 one suffers 13% of knocking cycles. The log-normal fitting function to describe such situation clearly shows a longer tail distribution towards high MAPO values, similarly to the outcomes in [14,15]. An additional assessment of knock severity is carried out using the Ringing Intensity index proposed in [27], for which a maximum limit of RI=5 MW/m^2 is adopted as heaviest acceptable knock [28]. For the SA12 condition a value of RI=4.1 MW/m^2 is obtained, confirming this as a knock-safe operation, while RI=26 MW/m^2 is obtained for the SA15 OP, attesting the not-tolerable knocking intensity of this condition for long engine runs.

Individual pre-ignition events are measured in the experiments, as shown in Figure 11 (Cycle no.160 and Cycle no.78, middle and bottom row), which are attributed to local deposits in the injector region (intake side) pre-igniting the fuel-air mixture and not by end-gas self-ignition (Cycle no.118, upper row), although the vast majority of cycles clearly shows end-gas self-ignition.

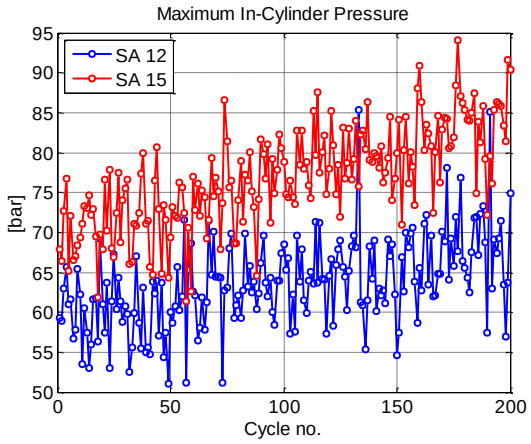


Figure 9. Cycle-specific peak pressure measured for SA12 and SA15 operations.

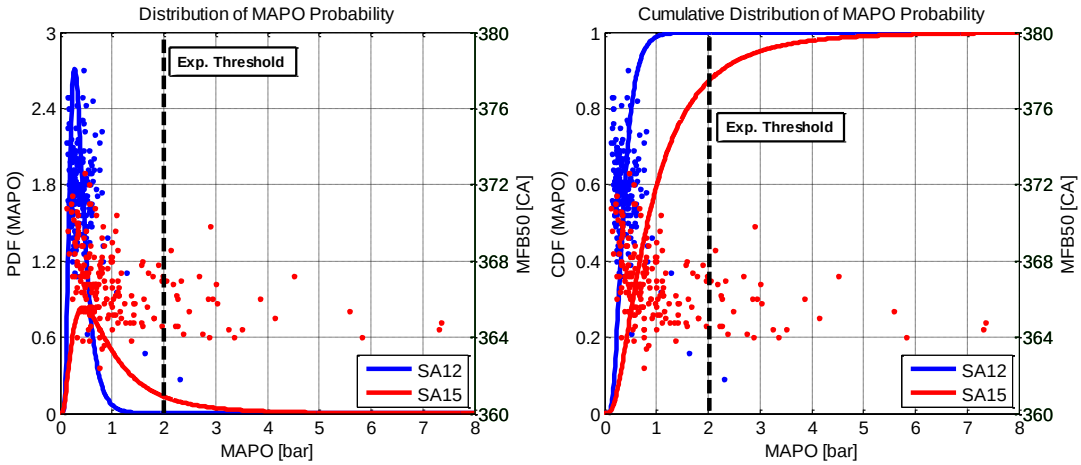


Figure 10. Cycle-resolved MAPO distributions for the SA12 and SA15 operations, together with the MFB50 phasing indicator. Superimposed are the log-normal distributions (left) and the cumulative probability (right) fitting curves of both experimental dataset.

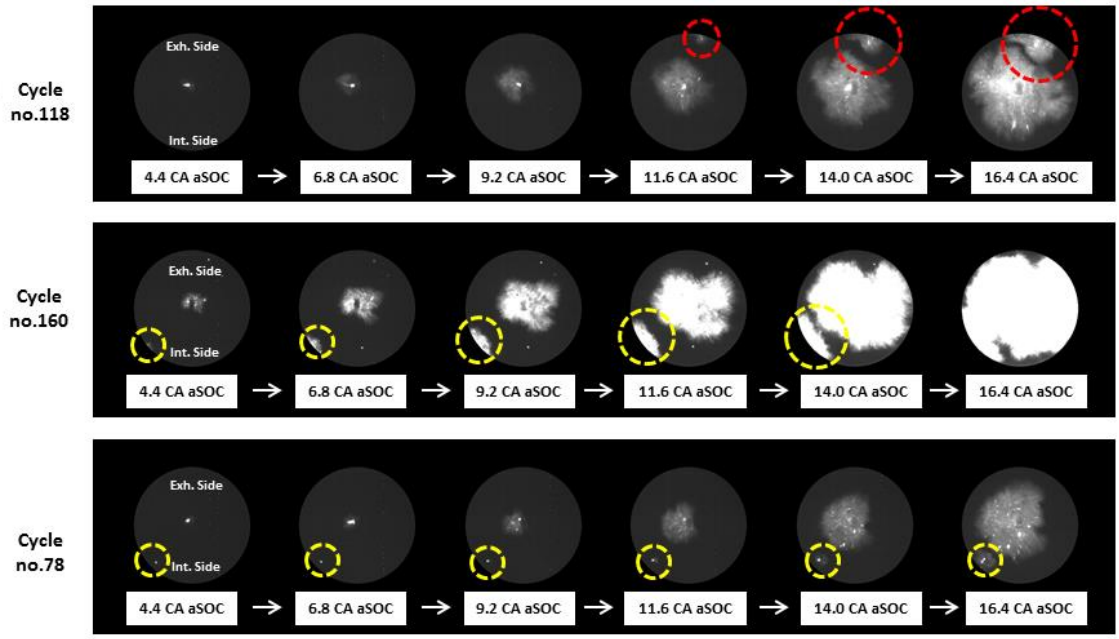


Figure 11. Flame front acquisition from the piston flat window for three high-pressure cycles. Cycle no.118 with end-gas self-ignition (upper row), while Cycle no.160 (middle row) and Cycle no.78 (bottom row) show early pre-ignition on the intake side.

Acquisition was initiated prior to spark timing in order to identify pre-ignition phenomena. Observed secondary flames were found to be correlated to pressure oscillations phasing and higher frequency of ignition sites was noted on the intake side [29]. Also, occurrences of secondary flames were much less evident for SA12 compared to the SA15 condition.

Numerical Setup

The 3D CFD simulations described in this paper are carried out by means of a customized version of STAR-CD v4.22, licensed by SIEMENS. Time dependent pressure boundary conditions are derived from the experiments and they are used to validate a 1D model of the engine, from which the corresponding temperature trace is extracted. Turbulence is modelled by means of the k-ε RNG turbulence model for compressible flows. The grid adopted for the simulations is reported in Figure 12 and thanks to symmetry it reproduces half of the combustion chamber with both one intake and one exhaust port. A close-up of the spark plug geometry and of the injector region are presented in Figure 12 as well. The total number of cells is approx. 1.7M and 0.8M at BDC and TDC respectively, while the average cell-size is about 0.55 mm throughout the simulation.

Spark-ignited combustion is modelled using the Flame Surface Density (FSD) based ECFM-3Z model [30], together with an energy-deposition ignition model based on a burnt gas profile deposition to account for flame kernel formation [31]. The modelling of the 6-hole full-cone GDI fuel injector follows the nozzle-specific orientation, which is imposed according to each of the six nozzle duct axes. The multi-hole liquid spray is modelled using a Lagrangian approach, where the primary fuel atomization is substituted by a Rosin-Rammler droplet distribution function. Nozzle-specific mass flow rate is imposed to reproduce the experimental flow unbalance measured between the nozzles. The effective nozzle diameter is estimated using the Kuensberg 1D model [32], while secondary break-up is modelled using the approach proposed by Reitz and Diwakar [33]. Finally, spray is validated against experiments carried out in a spray bomb at an injection pressure of 100 bar [10]. Given the wall-guided architecture, a liquid film model proposed by Senda et al. [34,35] is used for droplet-wall interaction. Wall temperatures are listed in Table 3 and they are imposed as region-specific boundary conditions derived from a validated 1D model.

Table 3. Wall Temperatures used in CFD simulations.

Piston Crown	450 K
Cylinder Liner	400 K
Cylinder Head	400 K
Intake Valve Stem	400 K
Intake Valve Face	420 K
Intake Port	380 K
Exhaust Valve Stem	570 K
Exhaust Valve Face	590 K
Exhaust Port	550 K

Finally, knock probability is modelled by means of the presented PDF-Knock model, which is coupled with the STAR-CD solver through in-house developed user-coding. A chemical mechanism for Toluene Reference Fuels (TRF) is used in this study to simulate the autoignition delay times of a RON95/MON85 commercial Gasoline. The mechanism is the one proposed by Andrae et al. [36], containing 138 species and for which a ternary blend of 16%/55%/29% n-Heptane/iso-Octane/Toluene mole fraction is defined as a surrogate fuel for RON95 Gasoline. A detailed analysis of the unburnt mixture statistical status will be the object of the next Section.

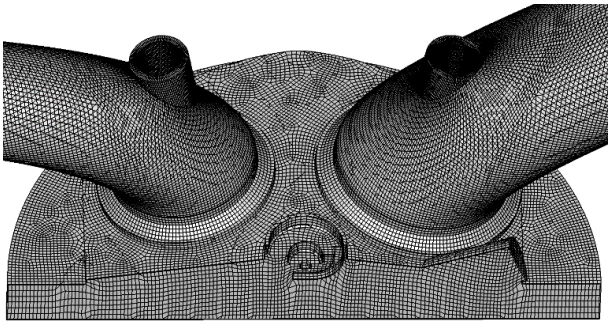


Figure 12. Computational grid at TDC.

Results

Combustion Simulation

Pressure traces for the sequence of 200 firing cycles for each OP are reported in Figure 13, together with their calculated ensemble average. In order to discard the effect of initial conditions on observed quantities, three consecutive cycles are simulated, and all the presented results pertain to the third cycle. Pressure traces from the CFD simulations as reported as well, and the agreement with the experimental ensemble average is the confirmation that the calculated RANS simulations accurately reproduce the mean burn rate for the two OPs.

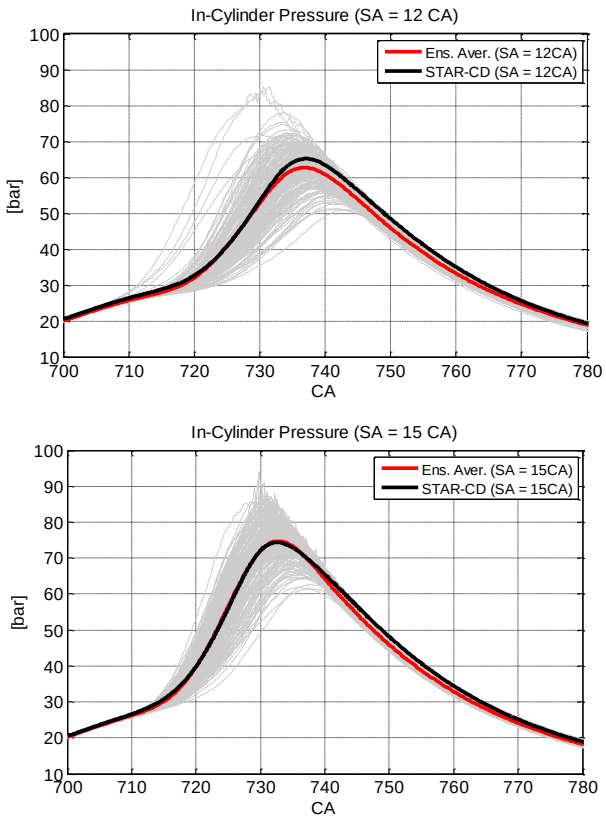


Figure 13. Cycle-resolved in-cylinder pressure from the experiments (grey thin lines), experimental ensemble average (red line) and RANS pressure trace (black line). Top: 12 CA bTDC; bottom: 15 CA bTDC.

The mean flame brush for the SA15 case is reported in Figure 14 by means of the $\tilde{c} \cdot (1 - \tilde{c})$ field, being $\tilde{c}$ the mass-based combustion progress variable. A large cycle-to-cycle variability is evident for both OPs, as well as individual cycles where pre-ignition possibly takes place. The distinct attitude towards knock is visible considering the upper bands of the experimental pressure trace envelopes. However, both 12CA and 15CA are knock-safe if the ensemble average pressure curve only is analysed. This is due to local pressure imbalance (i.e. the knocking pressure wave) which is measured by the pressure transduced but whose contribution is completely smeared out when phase-averaged with all the cycles present in the dataset. An analogous knock-safe prediction would result by standard RANS simulations of these two OPs, following the ensemble average rationale. This enforces the need to define more advanced (i.e. statistically-grounded) models to investigate knock occurrence in RANS simulations.

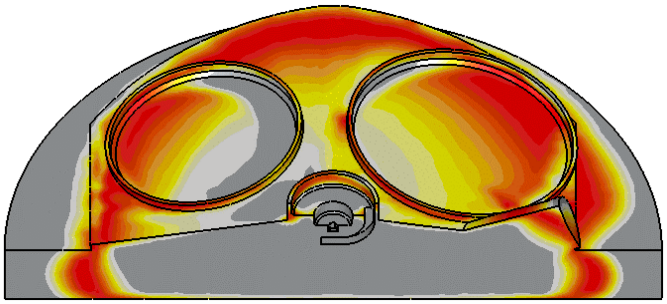
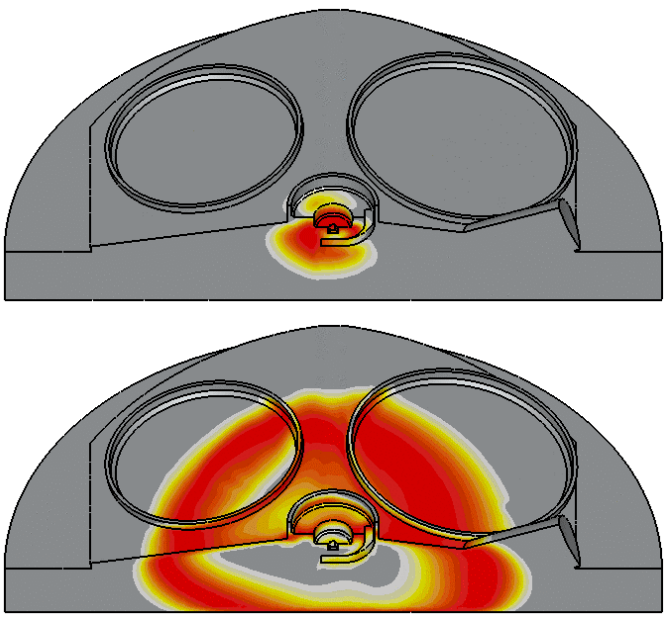


Figure 14. Turbulent flame brush $\tilde{c} \cdot (1 - \tilde{c})$ evolution: -10 CA aTDC (top), TDC (middle) and +10 CA aTDC (bottom).

Statistical Knock Prediction

Mean $\tilde{Z}$ and $\widetilde{T_u}$ fields are reported in Figure 15 at 450 CA, during the intake stroke and the fuel injection process. The mean $\tilde{Z}$ field (Figure 15, left) shows the wall-guided fuel jet impinging onto the flat piston crown, leading to liquid film formation and to a fuel-rich region adjacent to the piston crown. Spray evaporation is accompanied by a relevant charge cooling, as visible in Figure 15 (right) where a large temperature drop is present in the core-mixture; conversely, a relatively hot mixture is present on the exhaust side. Such mean mixture fraction and temperature fields are characterized by relevant gradients, generating variable variance. The variance fields of Z' and $T_u{}'$ are illustrated in Figure 16, highlighting variance peaks located in the high gradient regions: these are the spray jet peripheries for Z and the evaporation-cooled region for T_u.

Finally, the fields of turbulent Reynolds number Re_t and the related variance dissipation constant $c_t(Re_t)$ are reported in Figure 17, clearly stating the intensity of turbulence generation operated by the fuel spray, which acts as a local mixing promoter of temperature and fuel concentration gradients created by the spray itself.



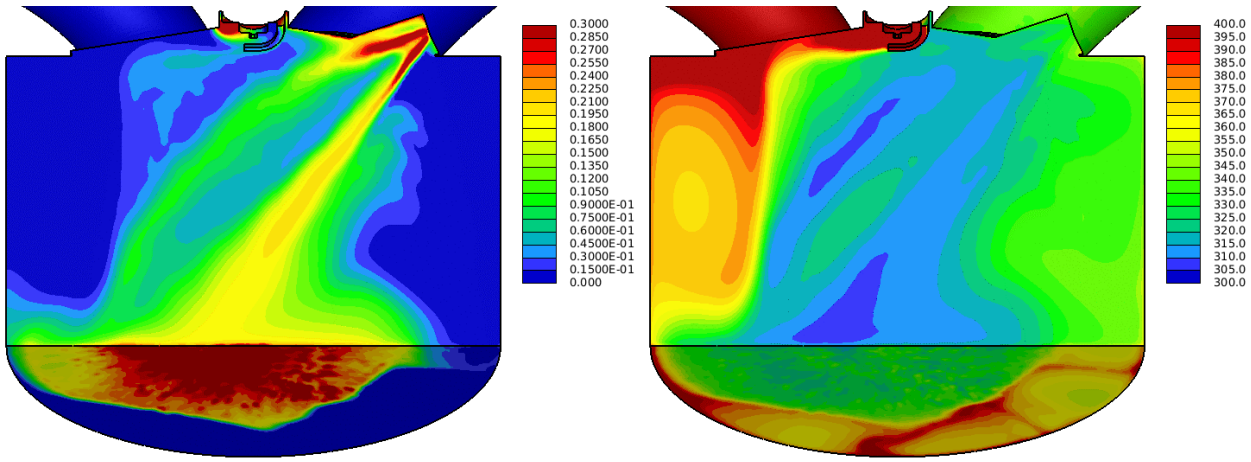


Figure 15. Field of mean mixture fraction $\tilde{Z}$ (left) and mean unburnt temperature $\widetilde{T_u}$ (right) at 450 CA.

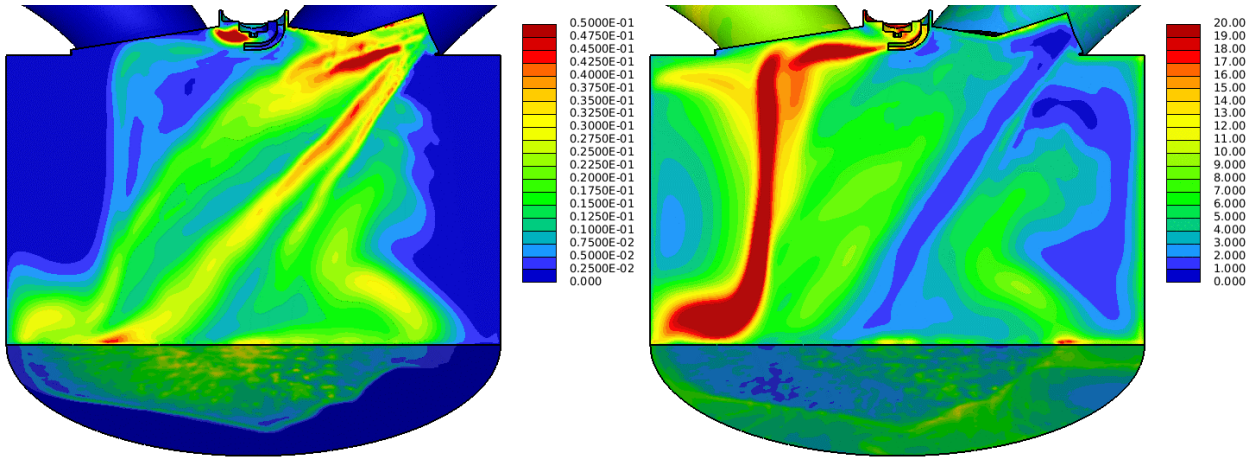


Figure 16. Field of mixture fraction variance Z' (left) and unburnt temperature variance $T_u{}'$ (right) at 450 CA.

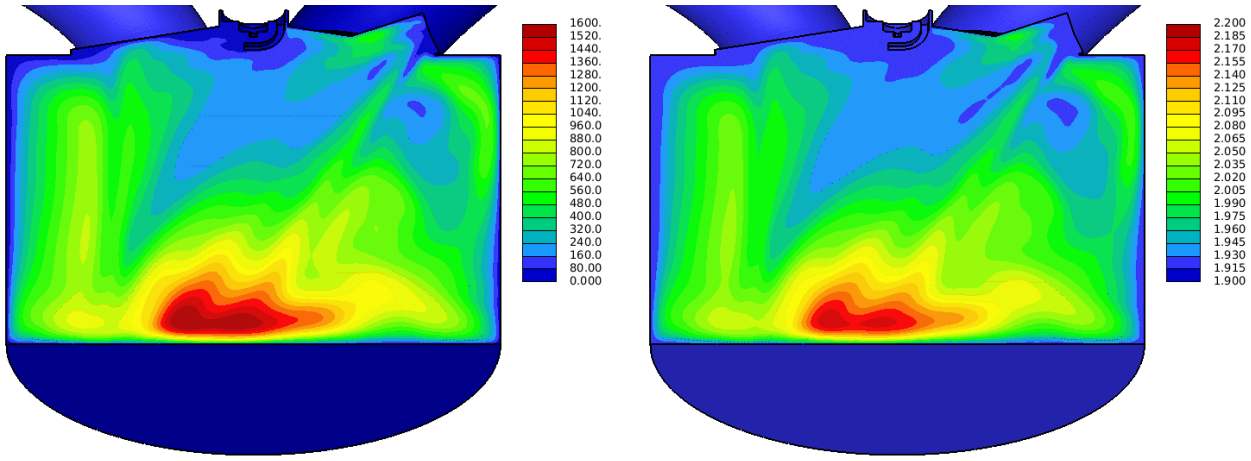


Figure 17. Field of turbulent Reynolds number Re_t (left) and variance dissipation constant $c_t(Re_t)$ (right) at 450 CA.

A detailed analysis of the end-gases is carried out for the SA15 case, being such condition representative of a knock-favorable case and a clear demonstrator of the knock statistical prediction. The analysis is performed at +10 CA aTDC, which is a timing close to the in-cylinder peak pressure, thus allowing the observation of the end-gas reaction rate at its maximum values.The average equivalence ratio and unburnt temperature fields are reported in Figure 18 on a section plane cutting 5 mm below the flame deck. It is clearly visible that from a thermal point of view, the exhaust side of the combustion chamber is the hottest area: this is mainly due to the presence of lean end-gas, thus lowering the specific heat and promoting charge heating due to piston compression. Therefore, the average most favorable knock onset location is the end-gas region on the exhaust side.

The root mean square (RMS) field of the equivalence ratio is calculated based on fuel stoichiometric AFR α_{st}, Z' and local oxygen and nitrogen concentration (Y_{O_2} and Y_{N_2}, respectively), as reported in Eq. 27 and illustrated in Figure 19 (top) on the same plane section.

$$\Phi' = \alpha_{st} \cdot \frac{Z'}{Y_{O_2}+Y_{N_2}} \qquad (27)$$

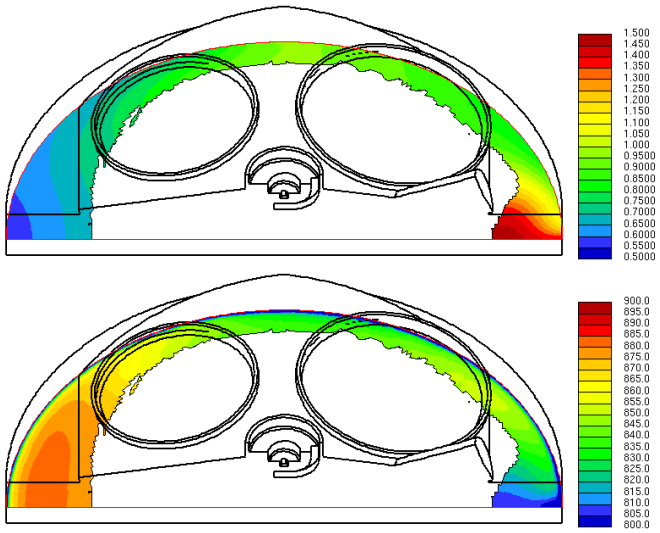


Figure 18. Field of mean equivalence ratio (top) and unburnt temperature (bottom) at +10 CA aTDC on a section plane 5 mm below the flame deck in the end-gas region.

Analogously, the temperature RMS field is obtained as square root of the T_u' field and it is illustrated in Figure 19 (bottom). It is visible that equivalence ratio variation is high in the exhaust valve region

and it reaches a maximum in the intake side end-gas. As for temperature variance, the near-wall gas region is systematically the one showing the highest T_u' values: this is due to the intense temperature gradients due to wall presence, combined with the reduced turbulence intensity and variance dissipation constant $c_t(Re_t)$. Both these considerations motivate the presence of high T_u' adjacent to the walls.

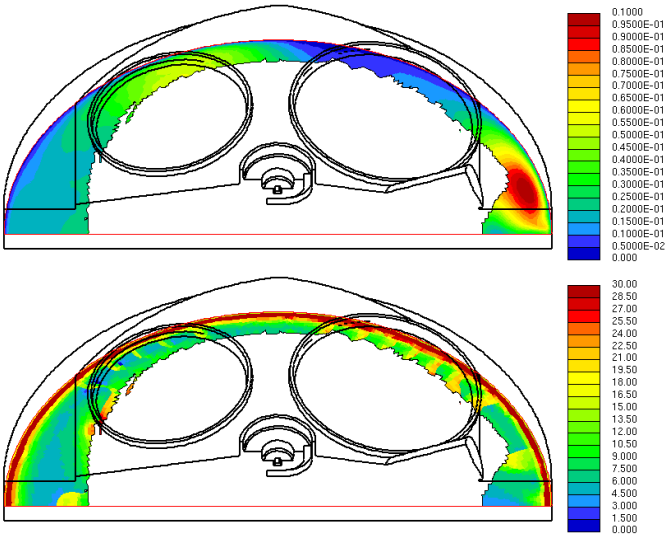


Figure 19. Field of Equivalence ratio RMS (top) and unburnt temperature RMS (bottom) at +10 CA aTDC on a section plane 5 mm below the flame deck in the end-gas region.

The turbulent Reynolds number Re_t and the variance dissipation constant $c_t(Re_t)$ in the end-gas region is reported in Figure 20 on the same section plane. Following Eq.4 and Figure 1, areas with high Re_t values are those where variance dissipation is promoted through high $c_t(Re_t)$ values, such as the exhaust side region in Figure 20. Therefore, turbulence-induced in-cell dispersion leads to higher variability in intake side end-gases, especially regarding mixture quality variance, while the exhaust side is relatively closer to a perfectly mixed condition, while low $c_t(Re_t)$ values at wall induce the mentioned $T_u{}'$ presence in near-wall regions.

The accelerating contribution given by the $\omega_{-\sigma}$ (Eq. 14) term characterizes points lying above the iso-reaction rate line, while the slow-down effect of the $\omega_{+\sigma}$ is responsible for the blue points below the 45-degree line. These are represented as the biased reaction rates $(\omega_{PDF,aver} + \omega_{-\sigma})$ and $(\omega_{PDF,aver} + \omega_{+\sigma})$, i.e. the calculated reaction rate deviation from the mean value $\omega_{PDF,aver}$ which are created by turbulence-related in-cell variances given by Eq. 2 and 3, finally leading to $\omega_{-\sigma}$ and $\omega_{+\sigma}$. The same is verified for both SA12 and SA15 OPs.

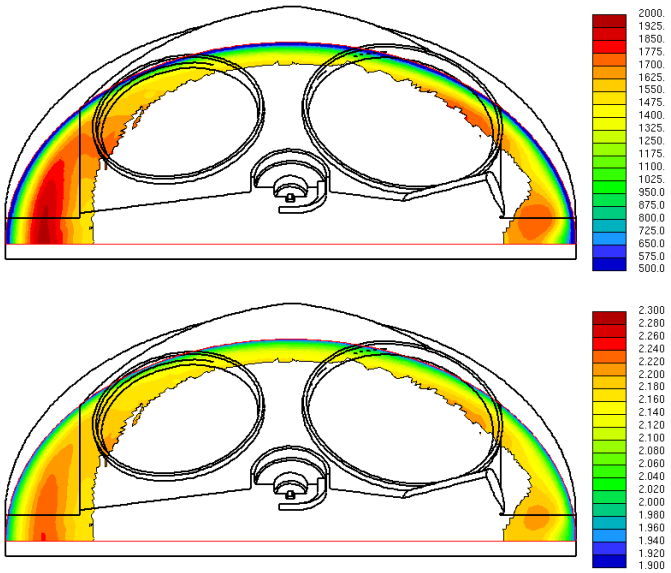


Figure 20. Field of turbulent Reynolds number Re_t (top) and variance dissipation constant $c_t(Re_t)$ (bottom) at +10 CA aTDC on a section plane 5 mm below the flame deck in the end-gas region.

Finally, the knock precursor iso-surfaces are illustrated in Figure 22 for the SA12 and SA15 conditions. The average knock precursor $I_{PDF-aver}$ never reaches the AI condition, i.e. unity, for both the SA12 and SA15 conditions. This is a confirmation that the average cycles are knock-safe for both OPs (see Figure 13). The experimental evidence confirms such statement, since sporadic knocking cycles are measured for SA12 (very rare events) and SA15 (few cycles). Since the average knock precursor $I_{PDF-aver}$ is not useful in such case, the focus is shifted to the peak knock precursor $I_{peak} = I_{PDF-aver} + I_{-\sigma}$. This is obtained as the sum of the knock precursor deviation towards knock ($I_{-\sigma}$, defined in Eq. 17) and the average precursor $I_{PDF-aver}$. This defines the regions where the inferred earlier knock probability may reach AI conditions.

The iso-surfaces of $I_{peak} = 1$ are reported in Figure 22, together with the mean flame front profiles, for both SA12 and SA15 conditions. Both simulations show $I_{peak} = 1$ spots, hence knock is statistically possible in both cases. The main knock region is found to be on the exhaust side (left side in the figures), where a large end-gas volume meets the earliest knock condition for both OPs. A second region of knock probability is identified on the intake side, where an analogous flame front retard and locally variant end-gas status lead to a probability to trigger knocking events.

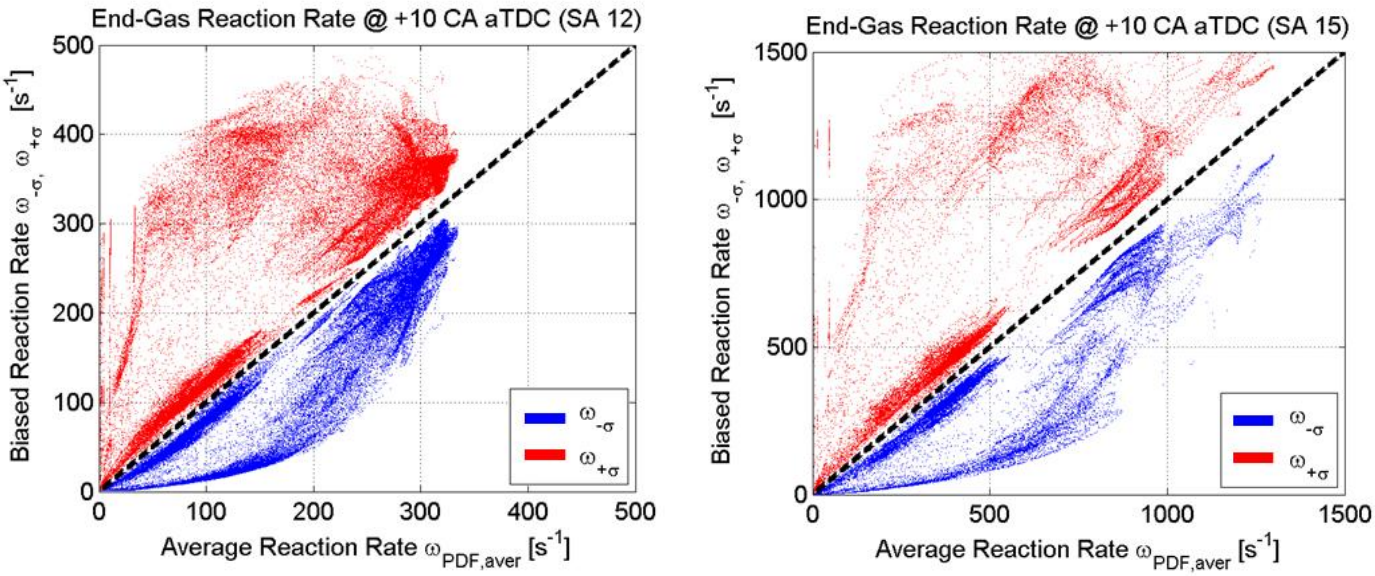


Figure 21. Biased reaction rate (i.e. maximum reaction rate, $\omega_{-\sigma}$, and minimum reaction rate, $\omega_{+\sigma}$) at +10 CA aTDC for the SA12 (top) and the SA15 (bottom) conditions.

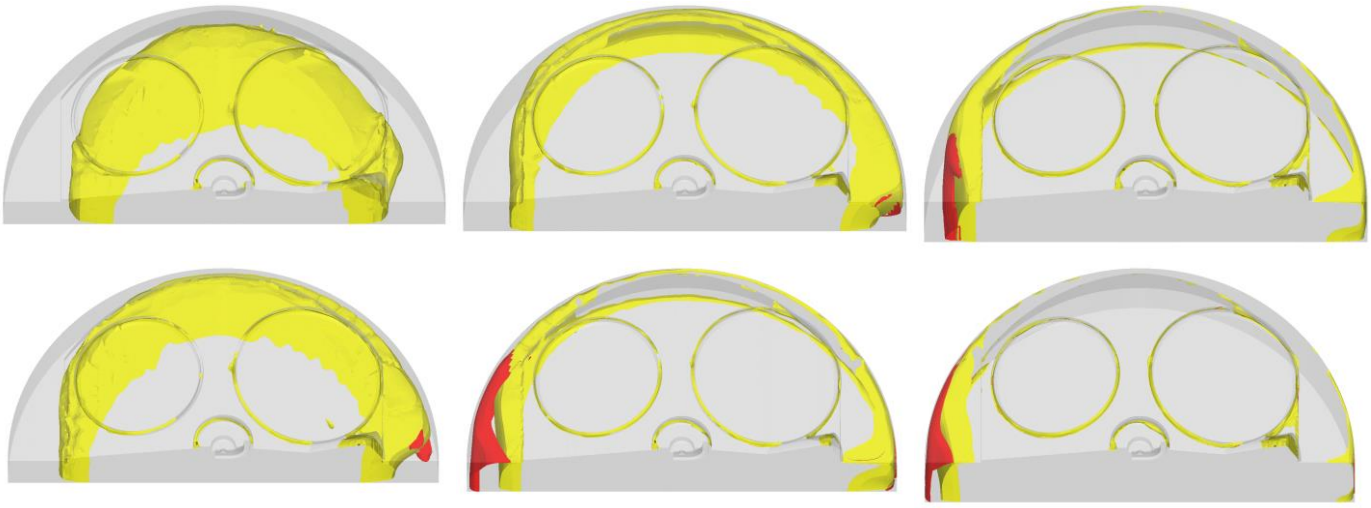


Figure 22. Isosurface of mean progress variable of combustion $\tilde{c} = 0.5$ (yellow) and of autoignition for the I_{peak} knock precursor (red). From left to right: +14 CA aTDC, +24 CA aTDC and +34 CA aTDC, for both the SA12 case (top row) and SA15 case (bottom row).

Probability of Knocking Cycles from the PDF-Knock Model for RON95 Gasoline

The final aim of the PDF-Knock model is to indicate an estimated probability of knocking cycles. Based on the knock indications given by the two independent knock precursors, namely the residual burnt fraction at knock onset $MFU_{\overline{KO}}$ and MFU_{KO},, the μ and σ parameters are obtained using Eq. 22 and 23. The estimated log-normal distribution of knock probability over the residual burnt fraction at knock (MFU_{KO}) is reported in Figure 23, together with the related CDF distributions. If compared to the experimental distribution of MAPO measurements in Figure 10, a remarkable similarity is found in log-normal PDF of knock index from the CFD simulations. In order to extend the number of simulated conditions for which the PDF-Knock model is tested, two additional spark advances are simulated, namely SA=18 CA bTDC and SA=21 CA bTDC (hereafter SA18 and SA21 conditions); these are reported in Figure 23. Although these OPs are not experimentally tested, due to the excessive knock intensity not tolerated by the research engine apparatus, they are interesting to the aim of analyzing the evolution of the knock distributions given by the PDF-Knock model.

In the experimental practice, a knock metrics and a threshold value for knock intensity must be defined in order to clearly distinguish knocking and knock-safe cycles. The same rationale is needed in the CFD simulations, i.e. a knock index must be defined. Coherently with the model rationale, knock intensity is expressed by the residual burnt fraction at knock onset. This is justified by the observation that higher engine damage is expected from early knocking events; moreover, the residual burnt fraction is part of several knock severity indices, such as the one proposed by Klimstra [23]. Regardless the index and the threshold that are adopted, the knock probability is the

area underlying the log-normal PDF above the threshold abscissa. It can be easily quantified by the related CDF curve, as the complement to unity for the threshold value (i.e. the remaining probability to 100%).

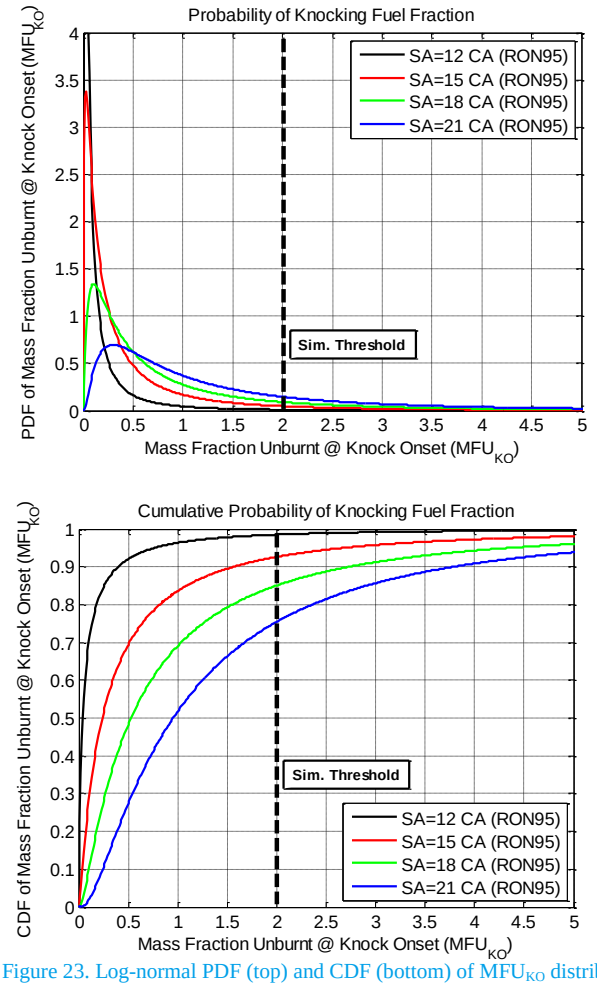


Figure 23. Log-normal PDF (top) and CDF (bottom) of MFU_{KO} distributions for four simulated SA for the RON95 gasoline.

A benchmark value for engine knock criterion for RANS simulation is MFU_{KO}=2%, i.e. 2% of the fuel fraction releasing heat by autoignition. Based on this limit, the presumed probability of knocking cycles is 1.5% for the SA12 case, increasing to 7.4% for the SA15 case. The 1.5% knock probability for the SA12 case is well comparable to an experimental knock-safe evidence, where 1%-2% of knocking cycles is considered as a maximum allowable value. As for the SA15 case, a probability of 7.4% is above the commonly adopted experimental thresholds, and coherently the PDF-Knock model predicts a statistically knocking condition even if the average cycles is knock-safe. The exact value of knock probability for the SA15 case (7.4%) is below the experimentally measured fraction for the same OP (13%). A first explanation of this is the presence of sporadic pre-ignition events in the experiments as shown in Figure 11, whose origin is different from end-gas AI and which are not accounted for by the PDF-Knock model; secondly, the model aim is to predict a probability of knocking cycles from flow statistics, and a satisfactory agreement with experimental trends is obtained.

Finally, the inferred knock probability grows to 14.9% and 24.6% for the SA18 and SA21 cases, for which experimental counterparts are not available but which show the typical log-normal shape bias towards earlier average knock (i.e. higher $MFU_{\overline{KO}}$) and increased variability of knocking events (i.e. higher $MFU_{KO\prime}$), amplifying the range of statistically presumed events.

To further generalize the PDF-Knock model outcomes, several threshold values are considered: MFU_{KO}=2%, MFU_{KO}=5% and MFU_{KO}=10%. The increase in the frequency of knocking cycles (hereafter KF) is non-dimensionalized on the frequency of the knock-limited case (SA12 in this case), and a knock Probability Growth Factor for increasing SA (defined as PGF, Eq. 28) is defined for each of the mentioned thresholds.

$$PGF = \frac{KF_{SA} - KF_{KLSA}}{KF_{KLSA}} \quad [\%] \tag{28}$$

This factor describes the amplification of the rate of knocking cycles when SA is increased from the knock-limited condition (KLSA, Knock Limited Spark Advance). The results for the RON95 case are shown in Figure 24, clearly stating that the knock frequency increase is independent on the specified threshold value for MFU_{KO}.

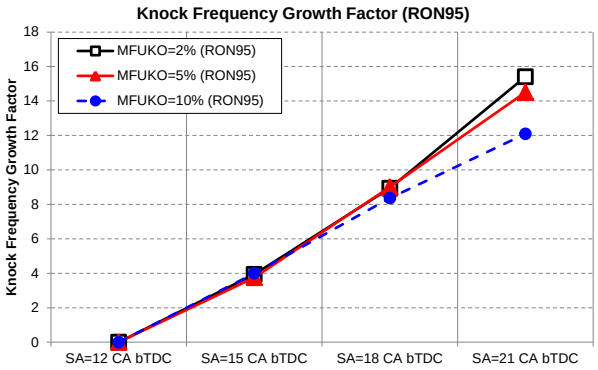


Figure 24. Knock Probability Growth Factor PGF for RON95 cases.

In particular, it is shown that the estimated frequency of knocking cycles grows 4 times every SA gain of 3 CA, independently from the specific MFU_{KO} limit value. This demonstrates the general character of the PDF-Knock model results and it is considered as a more relevant result than matching a predefined frequency of knocking cycles, since it describes a general model feature which can be coped with any knock intensity threshold or standard.

Probability of Knocking Cycles for RON91/RON98 Fuels

As a final step, a further demonstration of the PDF-Knock model potentiality is pursued by numerically simulating the same engine conditions with different gasoline qualities; both lower and higher anti-knock fuel qualities, namely RON91 and RON98, are tested. Three SA are analyzed for each of these fuels: SA is varied in the range 9-15 CA bTDC for RON91 given its low anti-knock quality, while SA values are increased for RON98 to 15-21 CA bTDC. These fuel models are obtained with the same mechanism adopted for the RON95 gasoline surrogate [36], with different blends to match the fuel-specific anti-knock quality. A ternary 17%/45%/38% n-Heptane/iso-Octane/Toluene mole fraction is used for RON91, while RON98 gasoline is modelled by a 9%/59%/32% n-Heptane/iso-Octane/Toluene mole fraction mixture.

The same procedure as the RON95 cases is followed and the log-normal PDF and CDF for such conditions is reported in Figure 25 and 26 for RON91 and RON98, respectively. Despite the retarded SA range for the RON91 fuel, a knock-safe condition is observed just for the SA=9 CA bTDC case; the engine abruptly enters in the knocking region when moving from SA=9 CA bTDC to SA=12 CA bTDC, this situation being amplified for the operation at SA=15 CA bTDC. For this last a probability close to 100% to measure knocking cycles is predicted. For the same limit of MFU_{KO}=2%, the presumed knock probabilities are 1.6%, 13.5% and 99% for the SA9, SA12 and SA15 respectively. The situation is the opposite for RON98 fuel, for which the SA15 condition is knock-safe, and moderate probability increase is predicted for SA18 and SA21 cases. Following the MFU_{KO}=2% limit, the presumed knock probabilities are 1.4%, 5.4% and 10.3% for the SA15, SA18 and SA21 respectively.

An overall resume of the knock probability for all the fuels and SA is reported in Figure 27. The use of the PDF-Knock model results useful especially in the red box region in Figure 27, indicating the OPs for which the ensemble average cycle is knock-safe: no information on their knock statistics could be inferred with a classic RANS knock approach, while the PDF-Knock model estimates a fraction of knocking cycles for these in the order of 10%. In order to detect knock in the average cycle, the OP must be moved in the blue region in Figure 27: it is evident to what extent the engine condition must be moved into the knocking region before knock is visible the average cycle, motivating the poor utility of such information.

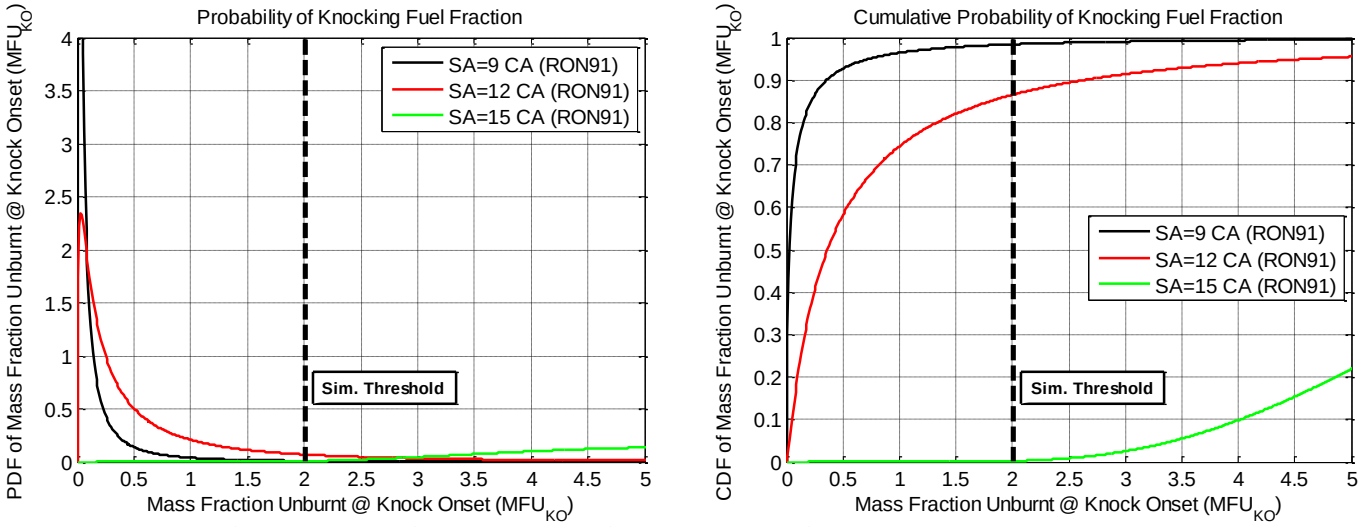


Figure 25. Log-normal PDF (left) and CDF (right) of MFU_{KO} distributions for three simulated SA for the RON91 gasoline.

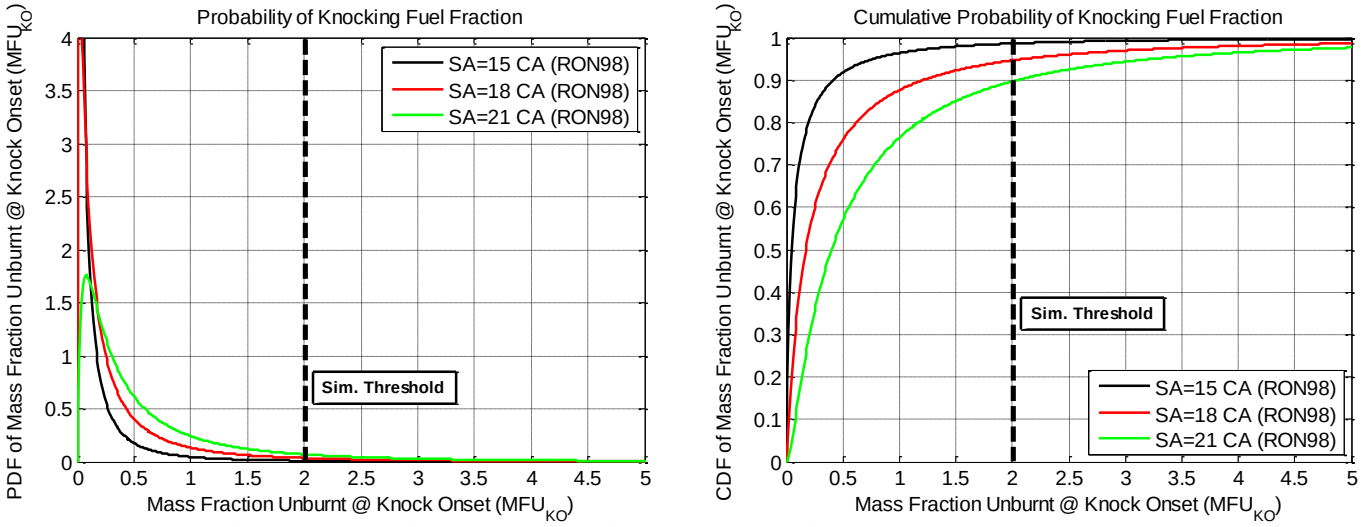


Figure 26. Log-normal PDF (left) and CDF (right) of MFU_{KO} distributions for three simulated SA for the RON98 gasoline.

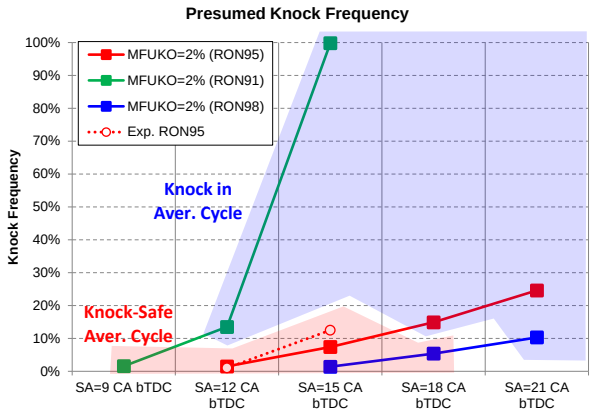


Figure 27. Presumed knock probability for RON95, RON91 and RON98 fuels for all the tested SA. Red region: OPs for which the ensemble average cycle is knock-safe; blue region: OPs where knock is detected in the average cycle.

The independence of the estimated knock frequency on the specific adopted threshold is repeated for the two additional fuels: once again, the knocking cycle frequency shows independency on the specific MFU_{KO} threshold, as reported in Figure 28. The slope of the PGF factor varies with the fuel type, being steeper for the RON91 fuel: a SA increase by 3 CA is extremely damaging for this low anti-knock fuel, markedly moving the engine condition in the knocking regime. A different trend characterizes the RON98 fuel: the frequency of knocking cycles increases just by a factor of 3 every 3 CA of SA increase. This means that the best anti-knock fuel is the less sensitive to SA variations.

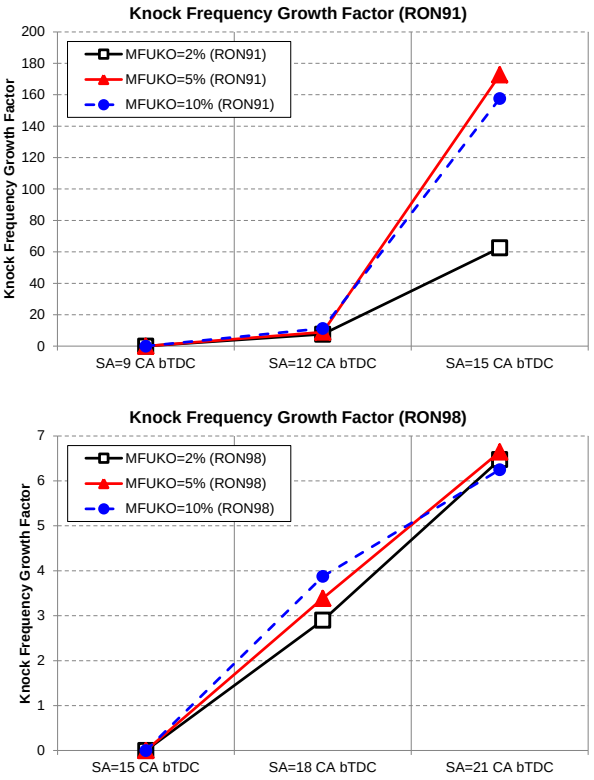


Figure 28. Knock Probability Growth Factor GPF for RON91 (top) and RON98 (bottom) cases.

Conclusions

In this paper, a PDF-based knock model for RANS simulations is presented. The model is based on the transport for mixture fraction and temperature variance through dedicated equations based on local turbulence intensity, allowing to reconstruct a statistical model of mixture reactivity for each computational fluid cell. The probability distribution of the in-cell reactivity is accounted for by separate knock precursors. To this aim, log-normal distributions are chosen as they provided a valuable description of knock intensity distribution during several experimental acquisitions. An analogous log-normal function formalism is used in the CFD simulations, where log-normal parameters are derived from the residual fuel fraction at knock onset, as predicted by the model knock precursors. The output of the PDF-Knock model is a presumed distribution of knock intensity, which can be compared to the experiments to define a threshold value.

The PDF-Knock model is then applied to a spark-sweep test on a single-cylinder research unit, where two SAs were experimentally tested for a RON95 gasoline. The RANS simulations confirm the experimental evidence, i.e. both conditions are knock-safe from an average point of view, although a non-negligible fraction of individual knocking cycles is estimated for the highest SA operation. The trend is further confirmed by numerical simulations of two SA increases over the experimental limit: the predicted frequency of knocking cycles increases steeply and the modelled shape of knock intensity distribution follows the experimental evidence for heavy knocking conditions.

Finally, the model behavior is tested for different anti-knock quality gasolines, RON91 and RON98 respectively, from knock-safe to heavy knocking conditions for both fuels. The fraction for knocking cycles increases more rapidly for the low-quality fuel (RON91), while the high-resistance fuel (RON98) tolerates better SA increase by slowly entering in the knocking domain. It is worthwhile to highlight that the amplification factor of the knock frequency for increasing SA is nearly independent on the selected threshold, making the model prediction of general use and suitable to be easily integrated in the industrial environment, where manufacturer's specific knock intensity thresholds are usually adopted.

The presented PDF-Knock model is shown to be able to predict not only the average but also a presumed probability of knocking cycles which is derived by transport equations and which closely matches the experimental trends. The results are obtained by a single RANS simulation, thus constituting a useful and physically-sound model for engine development process.

References

1. Dahnz, C., and Spicher, U., "Irregular combustion in supercharged spark ignition engines: Pre-ignition and other phenomena," International Journal of Engine Research 2010(11), 485-498.
2. Zhen, X., Wang, Y., Xu, S., Zhu, Y., Tao, C., Xu, T., Song, M., The engine knock analysis – An overview, Applied Energy 2012;92:628-36, doi:10.1016/j.apenergy.2011.11.079.
3. Robert, A., Richard, S., Colin, O., Martinez, L., De Francqueville, D., "LES prediction and analysis of knocking combustion in a spark ignition engine," Proceedings of the

Combustion Institute, Volume 35, Issue 3, 2015, Pages 2941–2948
4. Misdariis, A., Vermorel, O., Poinsot, T., “LES of knocking in engines using dual heat transfer and two-step reduced schemes,” Combustion and Flame, Volume 162, Issue 11, November 2015, Pages 4304–4312.
5. S. Fontanesi, A. d'Adamo, C.J. Rutland, Large-Eddy simulation analysis of spark configuration effect on cycle-to-cycle variability of combustion and knock, International Journal of Engine Research, April 2015; Vol. 16, 3: pp. 403-418., first published on January 9, 2015.
6. Fontanesi, S., Paltrinieri, S., D'Adamo, A., Cantore, G. et al., "Knock Tendency Prediction in a High Performance Engine Using LES and Tabulated Chemistry," SAE Int. J. Fuels Lubr. 6(1):98-118, 2013, doi:10.4271/2013-01-1082.
7. d’Adamo, A., Breda, S., Cantore, G., “Large-Eddy Simulation of Cycle-Resolved Knock in a Turbocharged SI Engine,” Energy Procedia 82 (2015) 45-50, doi:10.1016/j.egypro.2015.11.881.
8. S. Fontanesi, S. Paltrinieri, A. d'Adamo and S. Duranti, Investigation of Boundary Condition and Field Distribution Effects on the Cycle-to-Cycle Variability of a Turbocharged GDI Engine Using LES, Oil & Gas Science and Technology - Rev. IFP Energies nouvelles, Vol. 69 (2014), No. 1, pp. 107-128 DOI:10.2516/ogst/2013142.
9. d'Adamo, A., Breda, S., Fontanesi, S., and Cantore, G., "LES Modelling of Spark-Ignition Cycle-to-Cycle Variability on a Highly Downsized DISI Engine," SAE Int. J. Engines 8(5):2029-2041, 2015, doi:10.4271/2015-24-2403.
10. Breda, S., D'Adamo, A., Fontanesi, S., Giovannoni, N. et al., "CFD Analysis of Combustion and Knock in an Optically Accessible GDI Engine," SAE Int. J. Engines 9(1):641-656, 2016, doi:10.4271/2016-01-0601.
11. Forte, C., Bianchi, G.M., Corti, E., Fantoni, S., Costa, M., “CFD Methodology for the evaluation of knock of a PFI Twin Spark engine,” Energy Procedia 45 (2014) 859 – 868.
12. Linse, D., Kleemann, A., Hasse, C., “Probability density function approach coupled with detailed chemical kinetics for the prediction of knock in turbocharged direct injection spark ignition engines,” Combustion and Flame 161 (2014) 997-1014.
13. D'Adamo, A., Breda, S., Fontanesi, S., and Cantore, G., "A RANS-Based CFD Model to Predict the Statistical Occurrence of Knock in Spark-Ignition Engines," SAE Int. J. Engines 9(1):618-630, 2016, doi:10.4271/2016-01-0581.
14. Spelina, J.M., Peyton Jones, J. C., Frey, J., “Characterization of knock intensity distributions: Part 1: statistical independence and scalar measures, “Published online before print August 15, 2013, doi: 10.1177/0954407013496233, Proceedings of the Institution of Mechanical Engineers, Part D: Journal of Automobile Engineering February 2014 vol. 228 no. 2 117-128.
15. Spelina, J.M., Peyton Jones, J. C., Frey, J., “Characterization of knock intensity distributions Part 2: parametric models,” Published online before print August 23, 2013, doi: 10.1177/0954407013496234, Proceedings of the Institution of Mechanical Engineers, Part D: Journal of Automobile Engineering August 23, 2013 0954407013496234.
16. Leppard, WR, “Individual-cylinder knock occurrence and intensity in multi-cylinder engines,” SAE paper 820074, 1982.
17. Ferraro, CV, Millo, F., Fenoglio, C., et al. “A critical analysis of knock detection methods based on cylinder pressure analysis,” 1st international conference on control and diagnostics in automotive applications, Genova, Italy, 3–4 October 1996, pp. 293–304.
18. Millo, F. and Ferraro, C., "Knock in S.I. Engines: A Comparison between Different Techniques for Detection and Control," SAE Technical Paper 982477, 1998, doi:10.4271/982477.
19. Corti, E. and Moro, D., "Knock Indexes Thresholds Setting Methodology," SAE Technical Paper 2007-01-1508, 2007, doi:10.4271/2007-01-1508.
20. Livengood, J.C., Wu, P.C., Proc. Combust. Inst. 5 (1955) 347-356.
21. Fox, R. O., Computational models for turbulent reacting flows, Cambridge University Press, 2000.
22. Subramanian, G., Vervisch, L., and Ravet, F., "New Developments in Turbulent Combustion Modeling for Engine Design: ECFM-CLEH Combustion Submodel," SAE Technical Paper 2007-01-0154, 2007, doi:10.4271/2007-01-0154.
23. Klimstra, J. (1984) "The Knock Severity Index – A Proposal for a Knock Classification Method," SAE Technical Paper 841335, 1984, doi:10.4271/841335.
24. Merola, S., Irimescu, A., Marchitto, L., Tornatore, C. et al., "Flame Contour Analysis through UV-Visible Imaging during Regular and Abnormal Combustion in a DISI Engine," SAE Technical Paper 2015-01-0754, 2015, doi:10.4271/2015-01-0754.
25. Irimescu, A., Tornatore, C., Merola, S., and Valentino, G., "Combustion Process Investigation in a DISI Engine Fuelled with n-butanol Through Digital Imaging and Chemiluminescence," SAE Technical Paper 2015-01-1887, 2015, doi:10.4271/2015-01-1887.
26. Bowditch F. A new tool for combustion research a quartz piston engine. SAE Technical Paper 1961;610002. doi: 10.4271/610002.
27. Eng, J., "Characterization of Pressure Waves in HCCI Combustion," SAE Technical Paper 2002-01-2859, 2002, doi:10.4271/2002-01-2859.
28. Dec, J, Yang, Y, “Boosted HCCI for High Power without Engine Knock, and with Ultra-Low NOX Emissions using a Conventional Fuel,” 15th Directions in Engine-Efficiency & Emissions Research Conference, August 3 – 6, 2009, Dearborn, MI
29. Merola, S.S., Tornatore, C., Irimescu, A., "Cycle-resolved visualization of pre-ignition and abnormal combustion phenomena in a GDI engine," *Energ Convers Manage* 127:380-391, 2016, doi:10.1016/j.enconman.2016.09.035.
30. Colin O., Benkenida A. (2004) The 3-Zone Extended Coherent Flame Model (ECFM3Z) for computing premixed/diffusion combustion, Oil Gas Sci. Technol. – Rev. IFP 59, 6, 593-609.
31. Boudier, P., Henriot, S., Poinsot, T., Baritaud, T., “A Model for Turbulent Flame Ignition and Propagation in Spark Ignition Engines,” Twenty-Fourth Symposium (International) on Combustion/The Combustion Institute, 1992/pp. 503-510.
32. von Kuensberg Sarre, C., Kong, S., and Reitz, R., "Modeling the Effects of Injector Nozzle Geometry on Diesel Sprays," SAE Technical Paper 1999-01-0912, 1999, doi:10.4271/1999-01-0912.
33. Reitz, R. and Diwakar, R., “Effect of Drop Breakup on Fuel Sprays,” SAE Technical Paper 860469, 1986, doi:10.4271/860469.
34. Senda, J. and Fujimoto, H. 1999. 'Multidimensional modeling of impinging sprays on the wall of diesel engines', Appl Mech Review, 52, pp. 119-138.
35. Senda, J., Kanda, T., Al-Roub, M., Farrell, P.V., Fukami, T., and Fujimoto, H. 1997. 'Modeling spray impingement considering fuel film formation on the wall', SAE Paper 970047.
36. Andrae, J. C. G., and Head, R. A., “HCCI Experiments with gasoline surrogate fuels modeled by a semidetailed chemical kinetic model,” Combustion and Flame 156 (2009) 842-851.

Acknowledgments

The authors acknowledge and thank Prof. Peyton Jones for inspiring and fruitful discussion on knock probability distributions.

Contact Information

Alessandro d'Adamo, Ph.D.
Researcher
Department of Engineering “Enzo Ferrari”, University of Modena and Reggio Emilia
Via Vivarelli 10 - 41122 Modena (Italy)
Ph. +39 059 2056115
Fax: +39 059 2056126
alessandro.dadamo@unimore.it

Abbreviations

AFR	Air-to-Fuel Ratio
AI	Autoignition
aSOC	After Start of Combustion
aTDC	After Top Dead Center
BDC	Bottom Dead Center
CCV	Cycle-to-Cycle Variability
CDF	Cumulative Distribution Function
CoV	Coefficient of Variation
DI	Direct Injection
FSD	Flame Surface Density
KF	Knock Frequency
KLSA	Knock-Limited Spark Advance
KO	Knock Onset
LES	Large-Eddy Simulation
MAPO	Maximum Amplitude of Pressure Oscillations
MFB	Mass Fraction Burnt
MFU	Mass Fraction Unburnt
PDF	Probability Density Function
PGF	Probability Growth Factor
PSR	Perfectly Stirred Reactor
RANS	Reynolds-Averaged Navier Stokes
RMS	Root Mean Square
SA	Spark Advance
SI	Spark-Ignition
TDC	Top Dead Center
TRF	Toluene Reference Fuel